

PAPER

Verification of a quasi-linear model for gyrokinetic turbulent transport

To cite this article: G.M. Staebler *et al* 2021 *Nucl. Fusion* **61** 116007

View the [article online](#) for updates and enhancements.

You may also like

- [Stability and rockburst tendency analysis of fractured rock mass considering structural plane](#)
Yantian Yin, Huanxin Liu, Hanwen Jia et al.
- [Effect of Steam Curing on the Properties of High Early Strength Silica Fume Concrete](#)
Ramesh Nayaka, G S Diwakar and Virupaxappa Gudur
- [A Comparative Study on Seismic Analysis of Diagrid and Hexagrid Structural Systems](#)
Nachiar S Sindhu, S Anandh and A Mohamed Anas

Verification of a quasi-linear model for gyrokinetic turbulent transport

G.M. Staebler^{1,*}, E. A. Belli¹, J. Candy¹, J.E. Kinsey², H. Dudding³ and B. Patel^{3,4}

¹ General Atomics, San Diego, United States of America

² CompX, San Diego, United States of America

³ York Plasma Institute, University of York, United Kingdom of Great Britain and Northern Ireland

⁴ CCFE, Culham, United Kingdom of Great Britain and Northern Ireland

E-mail: Gary.Staebler@gat.com

Received 23 February 2021, revised 11 August 2021

Accepted for publication 7 September 2021

Published 23 September 2021



CrossMark

Abstract

The verification and calibration of a new quasi-linear transport model with a large database of gyrokinetic turbulence simulations is presented in this paper. In a previous paper (Staebler *et al* 2020 *Plasma Phys. Control. Fusion* **63** 015013), a model for the saturated spectrum of electric potential fluctuations was developed based on the properties of the non-linear 3D spectrum. In this paper, a modification to the overall multiplicative factor in this model is found to be necessary to improve the fit to scans of the temperature and density gradients. The error in the fit of the quasi-linear fluxes of electron and ion energy fluxes is significantly better than for previous saturation models. The spectral shift model for the impact of equilibrium $E \times B$ velocity shear (Staebler *et al* 2013 *Phys. Rev. Lett.* **110** 055003) and the zonal flow mixing model for electron-scale turbulence (Staebler *et al* 2016 *Phys. Plasmas* **23** 062518) are both revised to be compatible with this new model. The models for the loss of bounce averaging and electron collisions in the TGLF reduced linear equations (Staebler *et al* 2005 *Phys. Plasmas* **12** 102508) are also changed to improve the linear eigenmodes.

Keywords: tokamak transport, quasi-linear model, turbulence, gyrokinetic

1. Introduction

The quasi-linear approximation assumes the phase shifts that drive transport fluxes are determined by the most unstable linear eigenmodes [5]. This is generally found to be accurate for flux tube gyrokinetic turbulence simulations that saturate by mode coupling [6–8] and has been confirmed in experiments [9]. The quasi-linear approximation will be shown to be valid to high accuracy for a large database of gyrokinetic simulations in this paper. The saturated amplitude of the fluctuations of the fields and distribution function are small compared to their equilibrium by the same ordering parameter (frequency/ion gyrofrequency \approx ion gyro-radius/equilibrium gradient length) that was employed in the expansion of the Fokker–Plank equation to derive the gyrokinetic equation [10]. This small amplitude delta-f

approximation [11] follows from the balance of the non-linear mode coupling rate and the linear growth rate. A model of the saturated electric potential fluctuations, that multiply the quasi-linear weights (phase shifts), is sufficient to compute the transport fluxes driven by the turbulence in the quasi-linear approximation. The first mode-coupling saturation models were 0D using only a single poloidal wavenumber mode to compute the flux [12]. This was extended to 1D in the gyrofluid models GLF23 [13] and TGLF-SAT0 [14]. These models have each poloidal wavenumber eigenmode given a saturated intensity that is independent of the others in the 1D spectrum. They were the first models to be calibrated with non-linear turbulence simulations. A model that includes coupling between poloidal wavenumbers, mediated by zonal flow mixing, fits the 2D spectrum (radial and poloidal wavenumber) of the flux surface average saturated potential fluctuations including electron scale modes [3] (TGLF-SAT1). In this paper a new model (TGLF-SAT2), that includes the full 3D dependence (poloidal

* Author to whom any correspondence should be addressed.

angle, radial and poloidal wavenumber) of the saturated intensity [1], will be verified with a large database of gyrokinetic simulations.

The motivation for examining the poloidal angle dependence of the saturated intensity was the recent discovery that the periodic flux tube radial wavenumber (k_x) spectral code CGYRO [15] does not give the same dependence of the fluxes on flux surface elongation, and Shafranov shift, as the global radial grid code GYRO [16]. This difference was traced to the approximation for the gyro-average operator (Bessel function in k_x -space) mapping to the radial grid. This approximation is in common use for global gyrokinetic codes with radial grids. A complete Fourier transform of the radial grid in GYRO recovers the CGYRO results but this is expensive computationally. The approximate mapping was employed in the database of GYRO runs used to fit all previous saturation models for TGLF [17]. The new saturation model (SAT2) in this paper has geometric factors to match the results of the CGYRO simulations. The details of how these geometric factors were determined are given in a previous paper [1] where a new model for the saturated 3D spectrum of electric potential fluctuations from gyrokinetic turbulence simulations was presented. This model was built, for the first time, using the linear eigenmodes computed with the same gyrokinetic code (CGYRO [15]) as the non-linear simulations. This eliminates the uncertainty of the accuracy of the linear eigenmodes computed with a reduced model like TGLF [4]. The 3D potential fluctuation spectrum was examined, including the poloidal (k_y), and radial (k_x) wavenumbers, and the dependence on the poloidal angle (θ). The Miller geometry formalism for shaped toroidal magnetic flux surfaces [18, 19] was used. It was found that the geometric metrics of the perpendicular wave vector, normalized to the ion gyroradius at the local magnetic field strength, provided the functions needed to fit the poloidal angle dependence of the non-linear fluctuation intensity. These functions capture the flux surface shape dependence well. It will be shown in this paper, that this same model, with some re-calibration, fits a much larger set of gyrokinetic simulations.

The database of gyrokinetic simulations is described in section 2. Fundamental tests of the quasi-linear approximation are presented in section 3. The model for the saturation of the zonal (axisymmetric, $k_y = 0$) potential fluctuations is tested in section 4 and found to agree very well with the CGYRO cases. The details of the new model for the finite poloidal wavenumbers ($k_y > 0$) are presented in section 5. The verification and calibration of the saturation model to the CGYRO simulation database is presented in section 6. In section 7, improvements to the TGLF linear fluid equation models for electron collisions [20] and loss of bounce averaging [4] are presented. The implementation of the new (SAT2) saturation model in the quasi-linear TGLF transport flux calculation is verified with the CGYRO database in section 8. The spectral shift model [2] for equilibrium $E \times B$ velocity shear suppression of the turbulence is reformulated and simplified for the SAT2 model in TGLF in section 9. The zonal flow mixing model for electron scale turbulence [3] is also simplified and calibrated for TGLF-SAT2 in section 10. A summary is given in section 11 followed by an appendix A. The appendix A

discusses the transformation properties of quasi-linear fluxes and the summation measure for the fluxes.

2. Gyrokinetic turbulence simulation database

In order to verify and calibrate the saturation model, a set of 64 CGYRO turbulence simulations, composed of 13 scans about the GA standard (GASTD) case, were collected. The plasma parameters of the GASTD case are derived from tokamak L-mode conditions at mid-radius [13]. The scans cover most of the typical range of parameters found in the core region (inside the 80% flux surface) of L-modes and H-modes away for the kinetic ballooning mode threshold (i.e. low β). The GASTD case is well above the critical gradient for ion temperature gradient (ITG) modes and none of the scans, even at the lowest temperature gradient, enter into the non-linear Dimits shift regime [21] where the fluxes collapse for some parameter regimes. The quasi-linear approximation will be verified for all of the CGYRO simulations in this database. The parameters of the GASTD are: $a/L_{ne} = 1.0$, $a/L_{ni} = 1.0$, $a/L_{Te} = 3.0$, $a/L_{Ti} = 3.0$, $\hat{s} = 1.0$, $q = 2.0$, $\kappa = 1.0$, $r/a = 0.5$, $R/a = 3.0$, $\delta = 0.0$, $\Delta = dR/dr = 0.0$, $av_{ee}/c_s = 0.1$, $T_i/T_e = 1.0$, $\beta_e = 0.0005$. Note that finite electron collisions are included in this base case. There are 64 cases in this database but only 52 are unique. Most scans are for a single parameter but scans 12 and 13 vary magnetic shear and safety factor together such that $\hat{s} = q/2$. All are pure deuterium plasma with equal density, density gradients and temperature gradients for electrons and ions. Note that scan 7 is physical because the length 'a' is arbitrary and $r/R \leq 1.5/3.0$. The first two scans were used to determine the geometry dependence of the 3D saturation model [1]. Many of the rest of the scans were part of a study published by Belli *et al* [22]. The isotope dependence explored in this study will be addressed in a separate publication. The typical resolution used in these CGYRO turbulence simulations [22] is as follows: 16 toroidal modes, 128 radial modes, 8 energy nodes, 16 pitch angle nodes, 28 poloidal angles. The intervals between wavenumbers are $dk_y = 0.067$, $dk_x = 2\pi\hat{s}dk_y/BOX_SIZE$, $BOX_SIZE = 6$. The BOX_SIZE determines the number of independent extended ballooning modes in the simulation. The maximum ranges are $k_y = 1.005$ and $k_x = 10.67$ for most cases. The multi-species Sugama collision model [23] was used. Departures from the GASTD parameters held fixed for the scan are indicated in the last column of table 1. All of the CGYRO simulations were run long enough to fully saturate (at least $1200 a/c_s$ time units). The runs were inspected to make sure there were no slow secular trends in the fluxes over the time averaging window. The Miller flux surface geometry model is used [18]. Miller geometry is up/down symmetric so it does not exactly map to single null flux surface geometries. The new saturation model will need to be verified for general geometry in the future.

3. Fundamental tests of quasi-linear theory

The turbulent energy flux (Q_a) and particle flux (Γ_a) through a radial flux tube for the gyrokinetic simulation are computed

Table 1. CGYRO gyrokinetic turbulence simulation database.

Scan	Parameter	Range	Cases	Fixed
1	κ	1.0, 2.0	1–5	$\nu_{ee}a/c_s = 0.05$
2	Δ	0.0, –0.5	6–10	$\nu_{ee}a/c_s = 0.05$
3	ν_{ee}	0.05, 1.0	11–17	
4	a/L_T	1.25, 3.5	18–23	
5	a/L_n	0.0, 3.0	24–30	
6	ν_{ee}	0.5, 1.0	31–37	$a/L_n = 3.0$
7	r/a	0.25, 1.5	38–43	
8	R/a	2.0, 3.0	44–46	
9	T_i/T_e	0.5, 1.5	47–49	
10	\hat{s}	0.166, 1.5	50–54	
11	q	1.5, 3.0	55–57	
12	q	1.6, 4.0	58–61	$\hat{s} = q/2$
13	q	1.6, 3.0	62–64	$\hat{s} = q/2, a/L_n = 3.0$

for each species (subscript a) by the formulas

$$Q_a = \sum_{k_y} \sum_{k_x} \frac{3}{2} \left\langle \text{Re} \left[ik_y \frac{ae\tilde{\phi}_{k_x, k_y}^*}{\rho_s T_e} \frac{a\tilde{p}_{a, k_x, k_y}}{\rho_s n_e T_e} \right] \right\rangle_{t, \theta} = \sum_{k_y} Q_{ak_y} \quad (1)$$

$$\Gamma_a = \sum_{k_y} \sum_{k_x} \left\langle \text{Re} \left[ik_y \frac{ae\tilde{\phi}_{k_x, k_y}^*}{\rho_s T_e} \frac{a\tilde{n}_{a, k_x, k_y}}{\rho_s n_e} \right] \right\rangle_{t, \theta} = \sum_{k_y} \Gamma_{ak_y}. \quad (2)$$

Here the gyro-Bohm normalizations of the CGYRO code were used [15]: $c_s = \sqrt{T_e/m_D}$, a = minor radius at separatrix, $\rho_s = c_s/\Omega_s$, $\Omega_s = eB_{\text{unit}}/(m_D c)$, $B_{\text{unit}} = \frac{q d\psi}{r dr}$ [19] for poloidal magnetic flux ψ , and m_D = deuterium mass. The gyro-Bohm normalization for energy flux in these units is $n_e T_e c_s (\rho_s/a)^2$. The energy flux (equation (1)) is produced by a radial $E \times B$ drift driven by electric potential fluctuations ϕ_{k_x, k_y} that is averaged with the fluctuations of the pressure moment of the species distribution function (\tilde{p}_{a, k_x, k_y}). The angle bracket represents a time average (t) and a flux surface average over the poloidal angle (θ). There is also a sum over the normalized radial wavenumber (k_x) which is equivalent to a radial average over the periodic flux tube box.

The quasi-linear approximation to the turbulent flux evaluates the non-linear flux formula with the most unstable eigenmode at each poloidal wavenumber $\delta\phi_{k_y}$. Typically the most unstable eigenmode is for $k_x = 0$. The quasi-linear weights of a linear eigenmode are defined by

$$WQ_{ak_y}^{\text{QL}} = \frac{3}{2} \frac{\left\langle \text{Re} \left[ik_y \frac{ae\delta\tilde{\phi}_{k_y}^*}{\rho_s T_e} \frac{a\delta\tilde{p}_{a, k_y}}{\rho_s n_e T_e} \right] \right\rangle_{t, \theta}}{\left\langle \left| \frac{ae\delta\tilde{\phi}_{k_y}}{\rho_s T_e} \right|^2 \right\rangle_{t, \theta}} \quad (3)$$

$$WI_{ak_y}^{\text{QL}} = \frac{\left\langle \text{Re} \left[ik_y \frac{ae\delta\tilde{\phi}_{k_y}^*}{\rho_s T_e} \frac{a\delta\tilde{n}_{a, k_y}}{\rho_s n_e} \right] \right\rangle_{t, \theta}}{\left\langle \left| \frac{ae\delta\tilde{\phi}_{k_y}}{\rho_s T_e} \right|^2 \right\rangle_{t, \theta}}. \quad (4)$$

The quasi-linear approximation is valid if the phase angle between potential and velocity moments of the distribution

function in the non-linear turbulence preserves the linear eigenmode phase angles contained in the quasi-linear weights. This manifests itself as a preservation of the cross-phase between different velocity moments of the distribution function, like electron density and electron temperature, that have been measured in experiments [9, 24] and found to agree with non-linear and quasi-linear calculations. The phase preservation can also be tested in gyrokinetic turbulence simulations [6–8, 25]. In this paper the quasi-linear intensity spectrum needed to exactly match the electron energy flux will be computed. This will then be used to compute the ion energy and particle fluxes from their respective quasi-linear weights multiplying this intensity spectrum. The difference between these quasi-linear fluxes and the non-linear fluxes is a measure of the error in the quasilinear approximation originating from the quasi-linear weight. This test will be quantitatively verified for the cases in the database. Note that the small contribution due to the magnetic field fluctuations is not included in the CGYRO fluxes.

Because the non-linear flux contribution for each k_y are summed over k_x and flux surface averaged, it is not possible to directly compute the contribution to the electric potential fluctuation intensity from a single linear eigenmode. Instead, the quasi-linear intensity $I_{k_y}^{\text{QL}}$ required to make the quasi-linear flux exactly equal to the non-linear flux will be used. It is computed from the electron energy flux by the formula:

$$I_{k_y}^{\text{QL}} = \frac{Q_{ek_y}}{\Delta K_{iy} WQ_{ek_y}^{\text{QL}}}. \quad (5)$$

The poloidal wavenumber summation measure ΔK_{iy} is needed in equation (5) to make the intensity independent of the k_y grid. Note that an improved form of the interval was used in this paper which required some adjustments to the fitting parameters found in reference [1]. The summation measure is discussed in appendix A. If the quasi-linear approximation is valid, it should not matter which plasma species (subscript label $a = e, i$), or transport channel, is used to compute this intensity since the species dependence is accounted for in the quasi-linear weight. This is illustrated in figure 1 where the flux contribution to each poloidal wavenumber k_y is plotted for CGYRO (black) and the quasi-linear weight multiplied by $\Delta K_{iy} I_{k_y}^{\text{QL}}$ (gray) for ion energy flux (left) and particle flux (right). The electron energy flux match is exact by construction. For the GASTD case (top) the match for ion energy flux is good but the particle flux peak is lower for the quasi-linear flux indicating that the non-linear particle flux departs somewhat from the phase of the quasi-linear particle flux weight for this case. For a higher density gradient (bottom) the match is very good for both ion energy (left) and particle flux (right) in figure 1. Note that the particle flux is much higher for higher density gradient (lower right) than the lower density gradient (upper right). It is consistently found for the CGYRO database that the quasi-linear weight for particle flux is not as well preserved for low particle flux cases.

In order to be able to compare the error due to the quasi-linear weights with the errors reported below for the full quasi-linear flux model, the fractional error from using the quasi-linear intensity computed from the electron energy flux

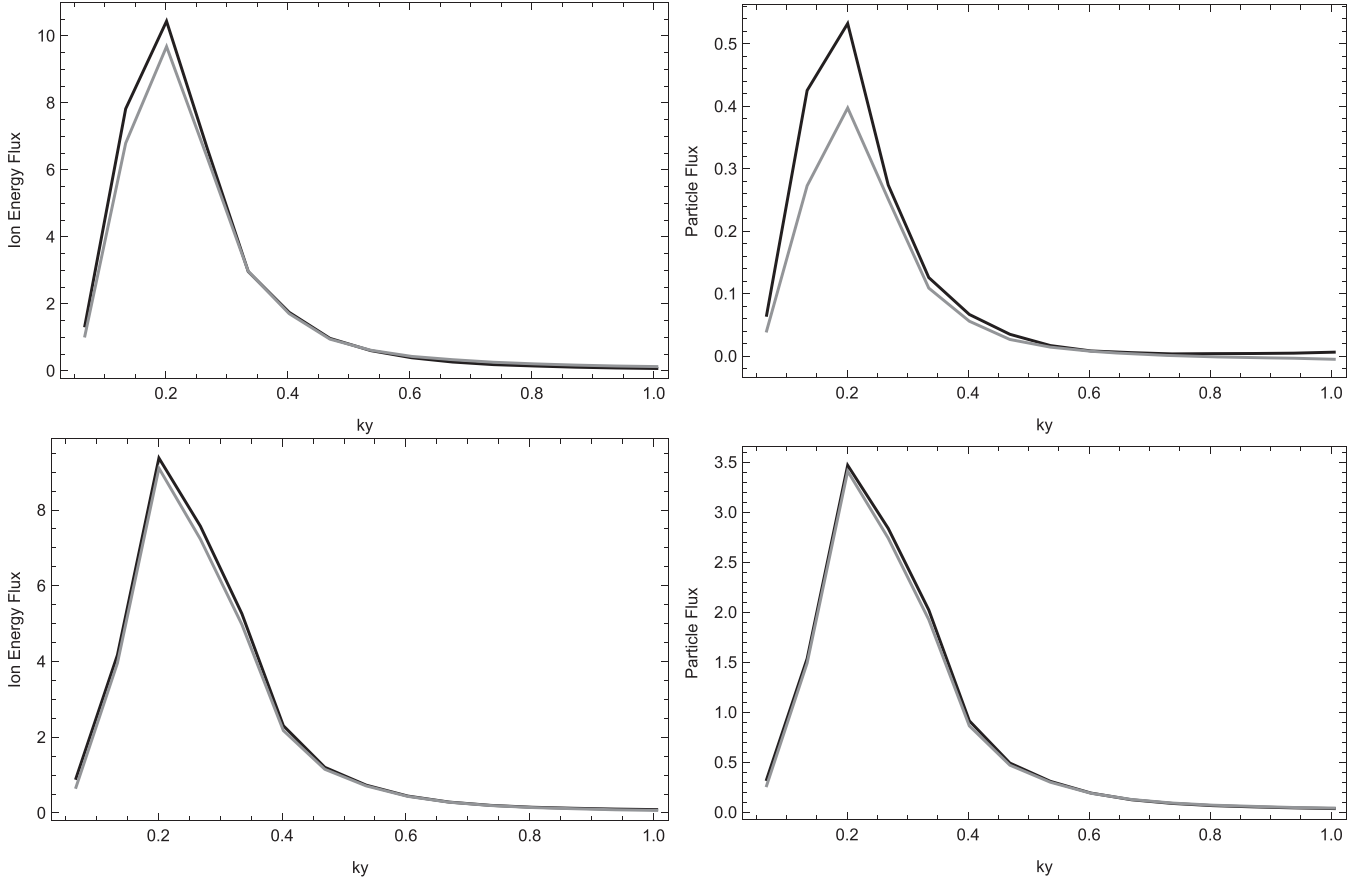


Figure 1. The ion energy flux (left) and particle flux (right) contributions for each k_y from the non-linear CGYRO runs (black) and computed from the quasi-linear weights (gray) times the intensity from the electron energy flux (equation (5)) for the GASTD case with density gradient $a/L_{n_e} = a/L_{n_i} = 1$ (upper) and 3 (lower).

(equation (5)) to compute the ion energy flux and particle fluxes for the database cases is computed in the following way:

$$\sigma_{WQ_i} = \sqrt{\frac{\sum_m \left(Q_i - \sum_{k_y} \Delta K_{iy} I_{k_y}^{QL} W Q_{ik_y}^{QL} \right)^2}{\sum_m Q_i^2}} \quad (6)$$

$$\sigma_{W\Gamma_e} = \sqrt{\frac{\sum_m \left(\Gamma_e - \sum_{k_y} \Delta K_{iy} I_{k_y}^{QL} W \Gamma_{ek_y}^{QL} \right)^2}{\sum_m \Gamma_e^2}}. \quad (7)$$

The summation index ‘ m ’ labels the members of each scan in the database (column 3 of table 1).

In figure 2 are shown the errors for the ion energy flux (left) and particle flux (right) for scans in the database. The root mean squared average error for the whole database is 5.4% for the ion energy flux and 19.8% for the particle flux. The high density gradient scans (6 and 13) have the lowest particle flux errors. These errors from the quasi-linear weights set a floor for the quasi-linear flux model since the model for the saturated intensity will have its own errors added in. The degree of error from non-linear departures from the quasi-linear weights is quite low for energy fluxes and particle fluxes of sufficient size.

4. Saturation of the zonal potential fluctuations

The time dependent zonal ($k_y = 0$) electric potential fluctuations play a strong role in the saturation of the gyrokinetic turbulence. Study of multi-scale (electron + ion gyroradius scales) turbulence simulations [26, 27] demonstrated that $E \times B$ flow shear due to the zonal potential could not compete with the linear growth rate at electron scales ($k_y > 1$). A new paradigm for saturation through zonal flow mixing [3] was proposed. The physical picture of the zonal flow mixing is like a washing machine agitator. The poloidal velocity of the fluctuating zonal $E \times B$ flow (V_{ZF}) cuts across the radial $E \times B$ velocity of the most unstable modes (finite k_y , $k_x = 0$) at a zonal flow mixing rate $V_{ZF} k_y$. Note that the zonal velocity couples modes with the same poloidal wavenumber k_y to modes with different radial wavenumbers k_x . This mixing can compete with the linear growth rate at all scales since the zonal flow mixing rate $V_{ZF} k_y$ scales with the poloidal wavenumber of the mixed mode. A simple detailed balance between the linear growth rate and the zonal flow mixing rate provides an estimate of the saturated amplitude of the RMS zonal flow velocity

$$V_{ZF} = \max[\gamma_{k_y}/k_y]. \quad (8)$$

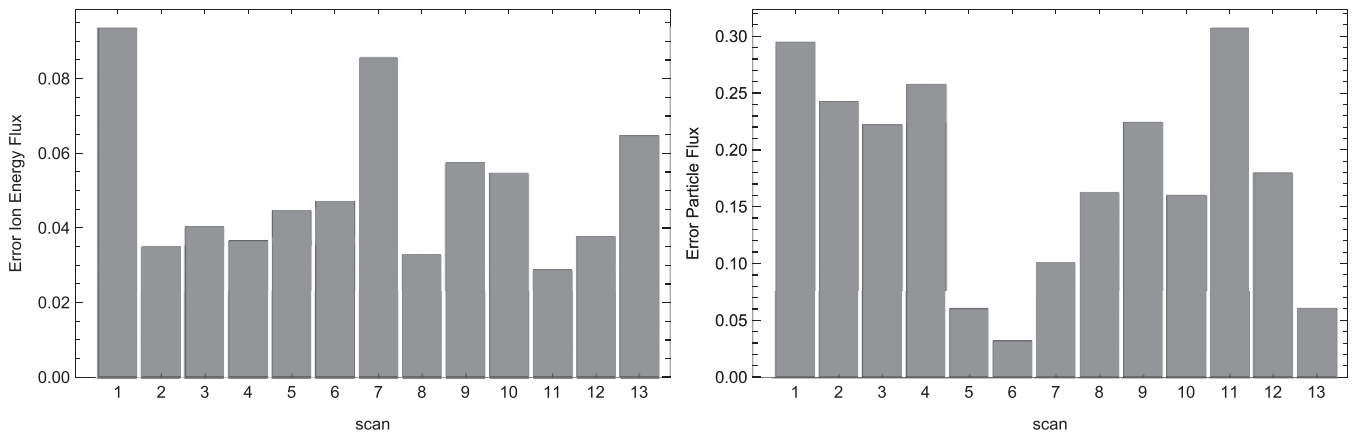


Figure 2. The error in the QL weight computed from the ion energy flux (left) and particle flux (right) for the 13 scans of the database table 1.

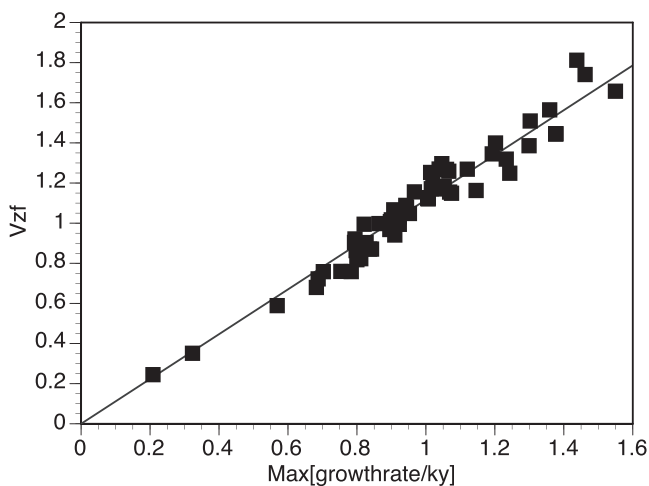


Figure 3. The RMS zonal velocity computed from the CGYRO simulations vs the maximum of the linear growth rate divided by the poloidal wavenumber.

Here, the linear growth rate γ_{k_y} (normalized by c_s/a) is for the most unstable mode at each k_y . The poloidal wavenumber ($k_{y\max}$) and growthrate (γ_{\max}) where the maximum drive for the zonal flows occurs (equation (8)) play an important role in the saturation model. The RMS zonal flow velocity can be computed directly from the non-linear saturated spectrum for $k_y = 0$

$$V_{ZF} = 0.5 \sqrt{\sum_{k_x} k_x^2 \left| \frac{ae\tilde{\phi}_{k_x, k_y=0}}{\rho_s T_e} \right|^2}. \quad (9)$$

The RMS zonal flow velocity V_{ZF} is independent of k_y so its saturated magnitude is set by the maximum drive in equation (8). This saturation rule for V_{ZF} (equation (8)) is shown to be well satisfied for the database in figure 3. The line in figure 3 is a fit to the data giving a linear coefficient of 1.12. Hence, the coefficient of 0.5 in equation (9) would be a better fit with 0.45. The saturation model, in the next section, for the finite k_y spectrum, does not depend on this coefficient. The lowest values of V_{ZF} are for the temperature gradient scan 4. The highest values are for scan 7 (r/a). A failure of the zonal flow saturation rule

(equation (8,9)), for a particular gyrokinetic simulation, would be an indication that zonal flow mixing is not the dominant saturation mechanism or that the simulation has not yet reached saturation. The scatter in figure 3 is lower using the CGYRO linear eigenvalues than it was in previous tests [3] where TGLF linear eigenvalues were used.

The RMS zonal flow velocity (equation (9)) is computed from the full zonal potential. However, there are typically static (zero frequency) zonal flows embedded in this spectrum. These can be extracted by time averaging the complex zonal potential. Transforming this static zonal potential to the radial coordinate used in CGYRO [15] ($0 \leq x \leq 2\pi$) gives the profiles illustrated in figure 4. There is typically a component to the static zonal potential from the longest wavelength radial mode (box mode) and a shorter wavelength corrugation. These corrugations are the distinctive static zonal flows observed in real space visualizations of gyrokinetic turbulence. As shown in figure 4, these corrugations can vary with plasma parameters significantly. The four cases shown are the GASTD case 1 (top left), the strong Shafranov shift ($\Delta = -0.5$) case 10 (top right) the weakest temperature gradient ($a/L_T = 1.25$) case 18 (bottom left) and the weakest magnetic shear ($\hat{s} = 0.167$) case 50 (bottom right) illustrate the variability in the simulations. The weak magnetic shear makes the corrugations longer wavelength and the Shafranov shift makes the corrugation very short wavelength.

The corrugation spectrum of the static zonal potential has isolated spikes only at the images of the most unstable extended ballooning mode (i.e. $k_x/(2\pi\hat{s}dk_y)$ is an integer). This is the type of spectrum expected from the ‘self-interaction’ mechanism for driving static zonal flows [28]. All of the cases in the database appear to have this type of spectrum that has been shown to be typical for kinetic electrons. Static corrugations have been observed in experiments [29] which is evidence that these corrugations are physical, rather than numerical artifacts. The RMS zonal flow velocities (equation (9)) computed from just the fluctuating part $V_{ZF-\text{fluc}}$ (squares), the static corrugation part $V_{ZF-\text{corr}}$ (triangles) and the static box mode part $V_{ZF-\text{box}}$ (diamonds) of the zonal potential are

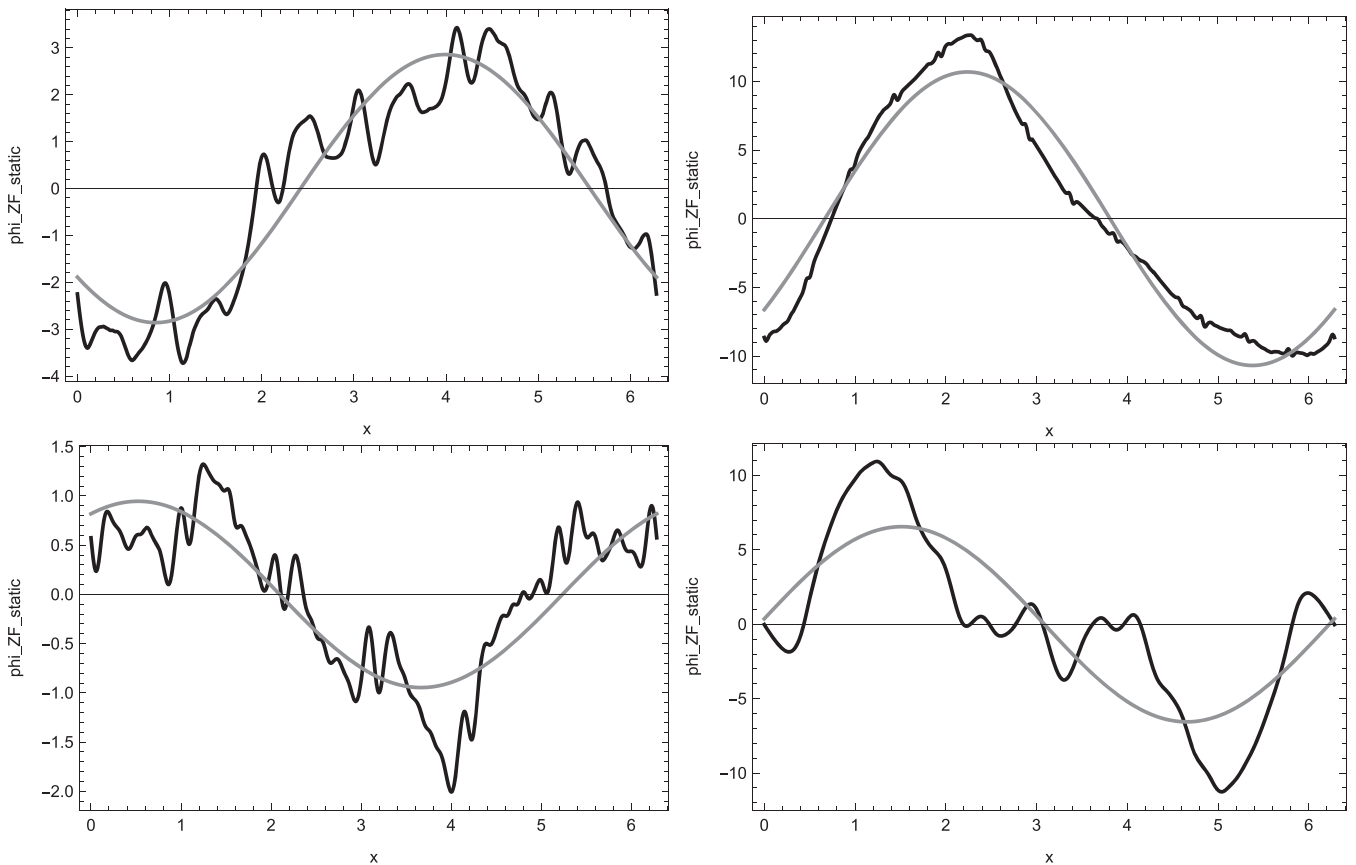


Figure 4. The time average zonal potential transformed to radial x -space (black) and the lowest k_x box mode (gray) for four cases: GASTD case 1 (top left), $\Delta = -0.5$ case 10 (top right), $a/L_T = 1.25$ case 18 (bottom left) and $\hat{s} = 0.167$ case 50 (bottom right).

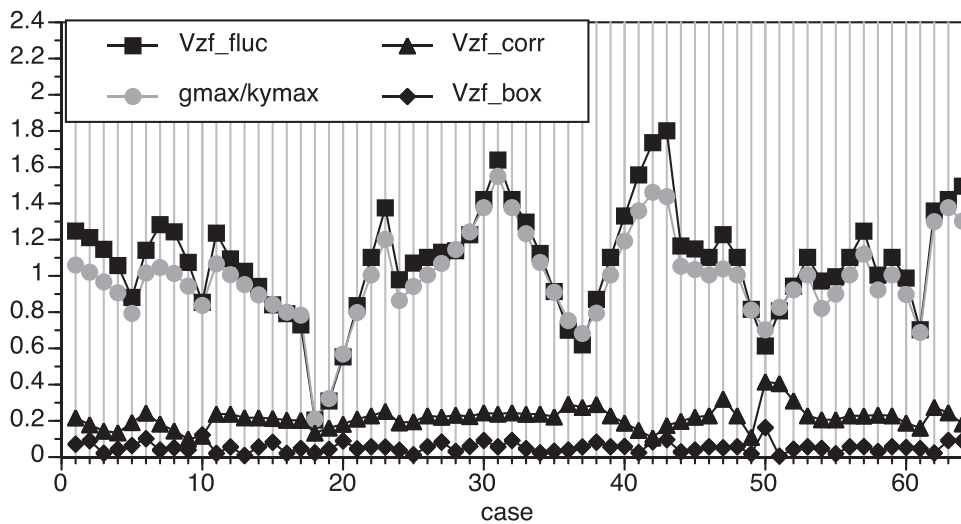


Figure 5. The RMS zonal velocity computed from the fluctuating (squares), static corrugations (triangles) and static box mode (diamonds) compared to the maximum of the linear growth rate divided by the poloidal wavenumber (circles) for all cases.

shown in figure 5. The fluctuating part tracks with the zonal flow saturation rule (equation (8)) very well and is usually the dominant contribution to the total RMS velocity. The contribution from the box mode is negligible. For case 18 (lowest temperature gradient) and case 50 (lowest magnetic shear) the static corrugation is making a significant contribution.

The static corrugation may play a role in the Dimits shift regime and deserves further investigation. The impact of the static zonal potential is usually assumed to be similar to an equilibrium sheared $E \times B$ velocity. Indeed, the novel new periodic method for including equilibrium $E \times B$ velocity shear in CGYRO [30] supports this viewpoint. The shear in

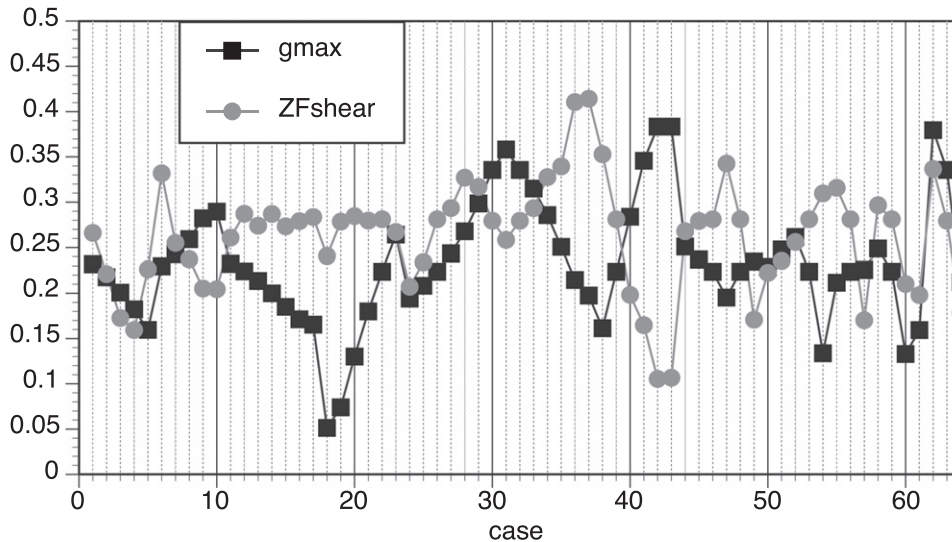


Figure 6. The static zonal flow shear (black) $ZF_{\text{shear}} = \gamma_{ZF}$ and the linear growthrate (gray) $g_{\text{max}} = \gamma_{k_{y\text{max}}}$ for all cases.

the static zonal flow can be computed from the formula

$$\gamma_{ZF} = 0.5 \sqrt{\sum_{k_x} k_x^4 \left\langle \frac{ae\tilde{\phi}_{k_x, k_y=0}}{\rho_s T_e} \right\rangle_t^2}. \quad (10)$$

Where the time average is indicated by $\langle \rangle_t$. This has the same units as the normalized equilibrium shear $\gamma_{EXB} = (a/c_s)(r/q)c d\phi_0/d\psi$ [31]. The time average zonal potential falls off strongly enough at high k_x that the summation in equation (10) converges. This summation diverges for the fluctuating zonal potential, making the definition of a shearing rate for the fluctuating zonal potential ambiguous. The static zonal flow shearing rate is compared to the linear growthrate at the maximum zonal flow drive $g_{\text{max}} = \gamma_{\text{max}}$ in figure 6. Although the static zonal flow shear is often larger than the linear growthrate, there is little correlation between them to indicate they are coupled. Hence, the role of the static zonal flow is not illuminated by this analysis. The zonal potential corrugation is known to be balanced by zonal pressure corrugations that can reduce the net impact [32] on local linear stability. Further study is required. The physical picture of zonal flow mixing, that the advection due to the fluctuating zonal potential balances the maximum linear drive (equation (8)) is supported by this analysis.

In the previous study of the 3D spectrum [1] it was observed that the RMS width of the radial wavenumber spectrum for finite k_y was limited to be larger than the width of the zonal potential spectrum. An accurate method for fitting the radial wavenumber spectrum with a Lorentzian model was employed to determine this width. The error in this fit tends to be larger for the zonal potential than the rest of the spectrum because the zonal potential spectrum sometimes narrows at low k_x [1]. For the first two scans, that were previously studied, the width of the zonal potential spectrum tracked the poloidal wavenumber at the maximum zonal flow drive $k_{xZF} \approx k_{y\text{max}}/|\nabla r|_0$ where the geometric factor is evaluated at the outboard midplane. For the wider database of this paper, it is found that this approximate

model needs to be generalized to:

$$k_{xZF}^{\text{model}} = 0.22 \sqrt{R/L_p} k_{y\text{max}} / |\nabla r|_0. \quad (11)$$

Here R is the major radius at the center of the flux surface, $R/L_p = -(R/P)dP/dr$ where P is the total pressure. This model is shown for all of the cases along with the spectral width $k_{xZF-\text{fluc}}$ computed from the fluctuating part of the saturated zonal potential spectrum in figure 7. The lowest width $k_{xZF-\text{fluc}}$ is for the temperature gradient scan 4 (cases 18–23). The highest widths are for high density gradient and high collision frequency (cases 36–37). The fit of the model is not tight but it is shown here because it motivates the pressure gradient factor needed to calibrate the overall fluxes to the CGYRO database that will be presented in the next section.

5. The new saturation model

The 3D model [1] for the saturated electric potential fluctuation amplitude $(\Phi(\theta))_{k_x, k_y} = ae|\tilde{\phi}(\theta)_{k_x, k_y}|/T_e \rho_s \sqrt{\Delta K_{iy}}$ has the functional form

$$\Phi(\theta)_{k_x, k_y} = G(\theta) \frac{\Phi(0)_{0, k_y}}{(1 + (k_x/k_x^{\text{RMS}})^2)}. \quad (12)$$

This form approximates the observed CGYRO spectrum. Here it is assumed that the peak of the spectrum $\Phi(0)_{0, k_y}$ is at $k_x = 0, \theta = 0$, which is true for the cases in this database. Note that the normalization of the fluctuation of the electric potential divides by the gyrokinetic expansion parameter ρ_s/a because the fluctuations are first order in this parameter (delta- f ordering). The RMS width of the radial mode number spectrum (k_x^{RMS} is computed at the outboard midplane ($\theta = 0$) by fitting the Lorentzian model distribution (equation (12)) to the non-linear spectrum. A model of the RMS width is given below ($k_x^{\text{model}} \approx k_x^{\text{RMS}}$). The effective non-linear mixing rate defined by

$$\gamma_{k_y}^{\text{eff}} = k_x^{\text{RMS}} k_y \Phi(0)_{0, k_y} \quad (13)$$

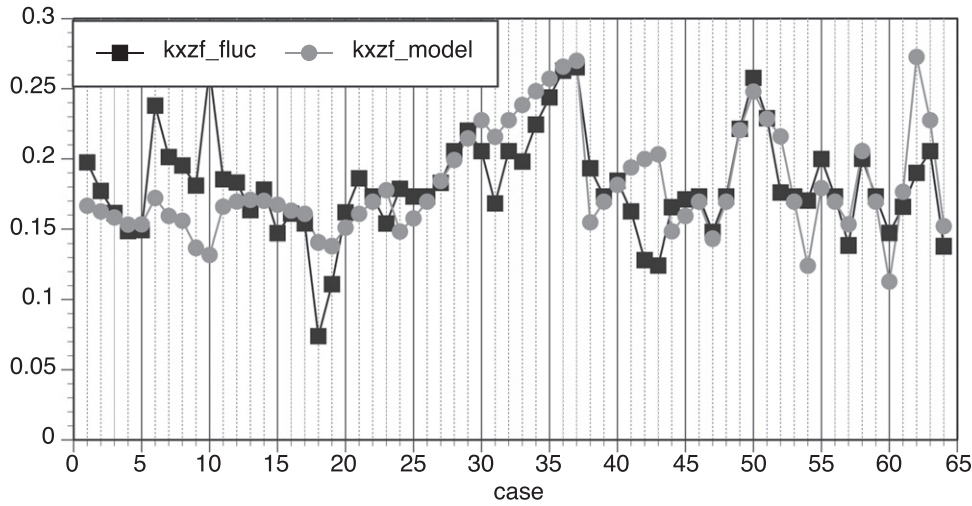


Figure 7. The RMS width of the zonal potential spectrum and the model equation (11).

is also computed directly from the non-linear spectrum. This has the dimensions of the non-linear $E \times B$ advection rate due to the finite k_y modes. A model for the effective mixing rate is given below ($\gamma_{k_y}^{\text{model}} \approx \gamma_{k_y}^{\text{eff}}$). All of the poloidal angle (θ) dependence is absorbed into the factor $G(\theta)$ that is fit to the amplitude of the peak potential fluctuation spectrum at $k_x = 0$ ($G(\theta) \approx \Phi(\theta)_{0,k_y} / \Phi(0)_{0,k_y}$).

The procedure used in reference [1] was to first construct the model of the 3D saturated electric potential intensity (equation (12)) and then reduce it to the quasi-linear intensity (equation (5)). The reduction takes a flux surface average of the 3D model and evaluates the 3D model at the peak ($k_x = 0$). This is consistent with the quasi-linear flux evaluation using a delta function distribution at the most unstable mode eliminating the sum over k_x . The final model for the saturated quasi-linear intensity spectrum is

$$I_{k_y}^{\text{model}} = \langle G^2(\theta) \rangle_{\theta} \left(\frac{\gamma_{k_y}^{\text{model}}}{k_x^{\text{model}} k_y} \right)^2. \quad (14)$$

This model transforms under a change in the external normalizations like the square of the normalized electric potential. This is an essential dimensional constraint on the allowed form of the model. The saturation model for the zonal flow velocity (equation (8)) determines the poloidal wavenumber $k_{y\text{max}}$ and linear growthrate γ_{max} at the peak of the zonal flow drive. These two quantities provide a natural reference wavenumber and growth rate that can be used to normalize the linear spectrum and recast the intensity spectrum in the form

$$I_{k_y}^{\text{model}} = \left(\frac{B_{\text{norm}} \gamma_{\text{max}}}{B_{\text{unit}} k_{y\text{max}}^2} \right)^2 \langle G^2(\theta) \rangle_{\theta} \hat{I} \left(\frac{k_y}{k_{y\text{max}}}, \frac{\gamma_{k_y}}{\gamma_{\text{max}}} \right). \quad (15)$$

The dependence on the external system of units is carried by the leading factor including an arbitrary choice of reference magnetic field B_{norm} . The other two factors are dimensionless in any system of units as is required for fitting by polynomials or a neural network. In general, it is desirable to not introduce any explicit dependence on the plasma parameters in the

model. The geometry factor and an overall pressure gradient factor introduced below are exceptions to this goal. In general, there can be more than one peak in the spectrum of γ_{k_y}/k_y . The dominant peak at ion scales is chosen for the model construction. The way the turbulence resolves the rare occurrence of multiple peak in the ion scale range is an open research question. There are known examples of gyrokinetic turbulence simulations where the electron scale peak drives the zonal flow velocity producing an electron scale $k_{y\text{max}}$ and very low ion-scale transport [33]. This possibility is currently excluded in the algorithm for selecting the ion scale peak to compute V_{ZF} from equation (8) pending further research.

Simple piece wise linear models were able to give a good fit for the 3 functions of k_y in this paper: $G(\theta)$, $\gamma_{k_y}^{\text{model}}$, k_x^{model} . The fitting coefficients are dimensionless constants independent of the system of external units.

The model for the shape function is

$$\begin{aligned} G^2(\theta) &= d_1 G_1(\theta) \quad \text{for } k_y < k_{y\text{cut}} \\ &= (d_1 G_1(\theta) k_{y\text{cut}} + b_3 d_2 G_2(\theta) (k_y - k_{y\text{cut}})) / k_y \quad (16) \\ &\quad \text{for } k_y \geq k_{y\text{cut}} \end{aligned}$$

where $b_3 = 1.0$ and the coefficients d_1, d_2 are

$$d_1 = \left(\frac{B_{T_0}}{B(0)} \right)^4 \frac{1}{|\nabla r|_0} \quad (17)$$

$$d_2 = 1/G_q(0)^2 \quad (18)$$

here $B(0)|_{r=0} = B_{T_0}$ is the toroidal magnetic field at the flux surface center and $G_q(\theta) = |\nabla r| B_{\text{unit}} / B(\theta)$. Two geometric shape functions are:

$$G_1 = \left(\frac{B(0)}{B(\theta)} \right)^4 \quad (19)$$

$$G_2 = \left(\frac{G_q(0)}{G_q(\theta)} \right)^4. \quad (20)$$

The cutoff is modeled by $k_{y\text{cut}} = b_0 k_{y\text{max}}$ where $k_{y\text{max}}$ is the value of k_y where γ_{k_y}/k_y is maximum and the best fit parameter was determined to be $b_0 = 0.76$.

The model (k_x^{model}) for the width of the potential radial wavenumber spectrum at finite k_y was fit to the RMS k_x width of the turbulence spectrum at the outboard midplane $\theta = 0$. The model is given by:

$$\begin{aligned} k_x^{\text{model}} &= \frac{B_{\text{unit}}}{B_{\text{norm}}} k_{y\text{cut}} / |\nabla r|_0 \quad \text{for } k_y < k_{y\text{cut}} \\ &= \frac{B_{\text{unit}}}{B_{\text{norm}}} (k_{y\text{cut}} / |\nabla r|_0 + b_1 (k_y - k_{y\text{cut}}) G_q(0)) \quad (21) \\ &\quad \text{for } k_y \geq k_{y\text{cut}}. \end{aligned}$$

Here B_{norm} is the arbitrary external magnetic field normalization which is chosen to be B_{unit} for CGYRO. The best fitting coefficient was determined to be $b_1 = 1.22$. This model differs from the previous saturation model (SAT1) [3] in that the k_x width does not continue to scale with k_y below $k_{y\text{cut}}$ but rather flattens out. This is conjectured to be the effect of the finite width of the zonal potential spectrum. There can be more complex structure to the k_x width in the region $k_y \leq k_{y\text{max}}$ that is not captured completely by this model. The dependence of the slope of k_x^{model} for $k_y \geq k_{y\text{cut}}$ on the geometric factor G_q was shown to be needed in reference [1].

The model for the effective non-linear mixing rate $\gamma_{k_y}^{\text{model}}$ in equation (14) is given by

$$\begin{aligned} \gamma_{k_y}^{\text{model}} &= b_2 \gamma_{k_y} \quad \text{for } k_y < k_{y\text{max}} \\ &= b_2 \gamma_{\text{max}} \quad \text{for } k_y \geq k_{y\text{max}} \end{aligned} \quad (22)$$

Here γ_{max} is the value of the linear growth rate at $k_{y\text{max}}$ where the peak in γ_{k_y}/k_y occurs. This model differs from the SAT1 model [3] in that it is simply b_2 times the linear growth rate for $k_y \leq k_{y\text{max}}$. The flattening of the k_x width model suppresses the intensity at low k_y making the zonal flow mixing subtraction included in SAT1 for $k_y \leq k_{y\text{max}}$ unnecessary. The observed flatness of the non-linear mixing rate above $k_{y\text{max}}$ is consistent with strong mixing between different poloidal wavenumbers in this range distributing the fluctuation intensity. In the electron range of k_y an explicit poloidal wavenumber mixing is needed in order to match the intensity spectrum as shown in section 10.

The reader is referred to reference [1] for the procedure used to determine this model from the 3D potential spectrum properties. The four fitting coefficients (b_0, b_1, b_2, b_3) were adjusted to minimize the absolute RMS difference between the CGYRO and the quasi-linear model energy flux contributions at each k_y for the first two scans in the database. The coefficients b_0 and b_3 have been adjusted due to an improvement made to the summation measure as discussed in appendix A. In order to fit the wider database of this paper, it was found that the overall coefficient needed to be modified to

$$b_2^2 \rightarrow 3.74 \left(\frac{12L_p}{R} \right). \quad (23)$$

The value 3.74 is determined by forcing the offset from CGYRO in the sum of electron and ion energy fluxes to be zero

for the whole database. This modification may be related to the trend for the width of the zonal potential spectrum found in equation (11) since $\sqrt{R/L_p} \approx k_{x\text{ZF}} |\nabla r|_0 / k_{y\text{max}}$. Note that the GASTD case ($R/L_p = 12$) is taken as a reference point. Alternatives to the pressure gradient factor were tried as discussed in the next section.

6. Verification and calibration of the quasi-linear fluxes

The quasi-linear model fluxes are computed from the formulas:

$$Q_a^{\text{QL}} = \sum_{k_y} \Delta K_{iy} I_{k_y}^{\text{model}} W Q_{ak_y}^{\text{QL}} \quad (24)$$

$$\Gamma_a^{\text{QL}} = \sum_{k_y} \Delta K_{iy} I_{k_y}^{\text{model}} W \Gamma_{ak_y}^{\text{QL}}. \quad (25)$$

The linear growth rate and quasi-linear weight spectrum are computed using CGYRO. The fractional error for these quasi-linear fluxes compared to the CGYRO fluxes is computed for each scan by the formula:

$$\sigma_{Q_a^{\text{QL}}} = \sqrt{\frac{\sum_m (Q_a - Q_a^{\text{QL}})^2}{\sum_m Q_a^2}} \quad (26)$$

$$\sigma_{\Gamma_a^{\text{QL}}} = \sqrt{\frac{\sum_m (\Gamma_a - \Gamma_a^{\text{QL}})^2}{\sum_m \Gamma_a^2}}. \quad (27)$$

The fractional errors for all of the database scans are given in figure 8. The RMS average of these errors is 10.5% for Q_i , 10.9% for Q_e and 18.9% for Γ_e . These are almost a factor of 2 lower errors than previous saturation models and may be within the uncertainty of the gyrokinetic simulations due to finite time averaging and grid resolution. The particle flux error due to the quasilinear weights (19.8%) is the primary contribution for this channel. The quasi-linear weight error is about half of the total error for energy fluxes.

In figure 9 are plotted the ion energy flux (top) electron energy flux (middle) and particle flux (bottom) for CGYRO (black) and the QL model (gray) for all of the 64 cases in the database. The cases are numbered sequentially in the order they appear in the database table 1.

The modification of the overall fluxes with pressure gradient was needed for the scans in temperature gradient (4) and density gradient (5). These scans could also be fit by modifying the overall coefficient to vary with the ratio of γ_{max} to a proxy for the geodesic acoustic mode frequency v_{thi}/R such that the quasi-linear intensity scaled like the first power of γ_{max} instead of the second power. However, this choice spoils the good agreement with other scans (e.g. collisions, magnetic shear). The pressure gradient factor can also be replaced by a factor involving the convection fraction of the total energy flux. This works well for all cases except the major radius scan 8. The pressure gradient factor essentially changes the flux surface label from 'r' to 'P' in the linear gradient drift terms. Since the total pressure gradient is fundamental to the radial force balance of the plasma, it defines a spacing between flux surfaces that perhaps has an impact on the turbulence. It

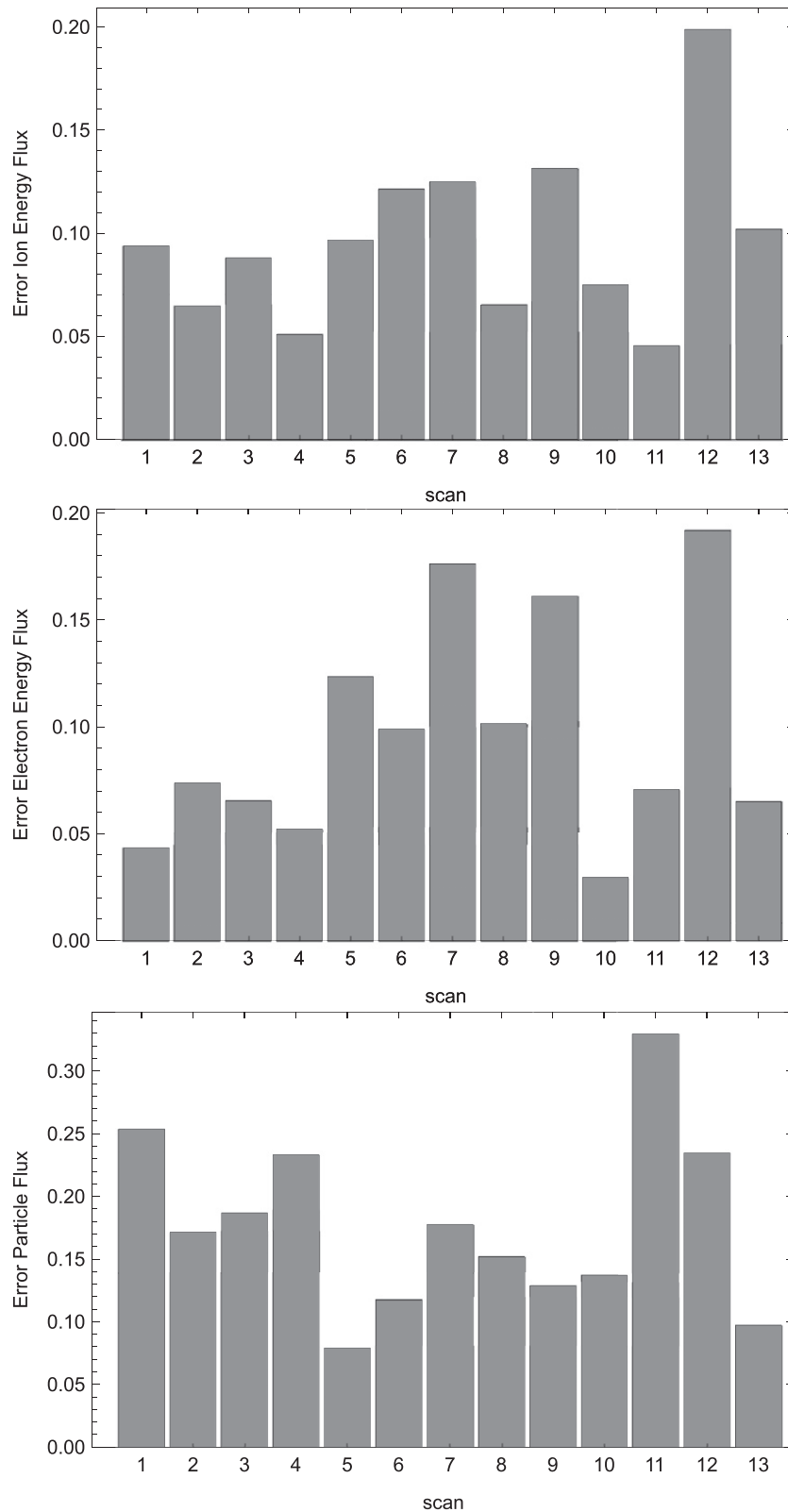


Figure 8. The fractional error equations (26) and (27) for the 13 scans in the CGYRO database table 1. Ion energy flux (top), electron energy flux (middle) and particle flux (bottom).

is the unique gradient scale length for the force balance equilibrium. If this is an equilibrium effect, then the total pressure

including fast ions should be used. This needs to be verified. The pressure gradient factor is introduced to improve the fit for

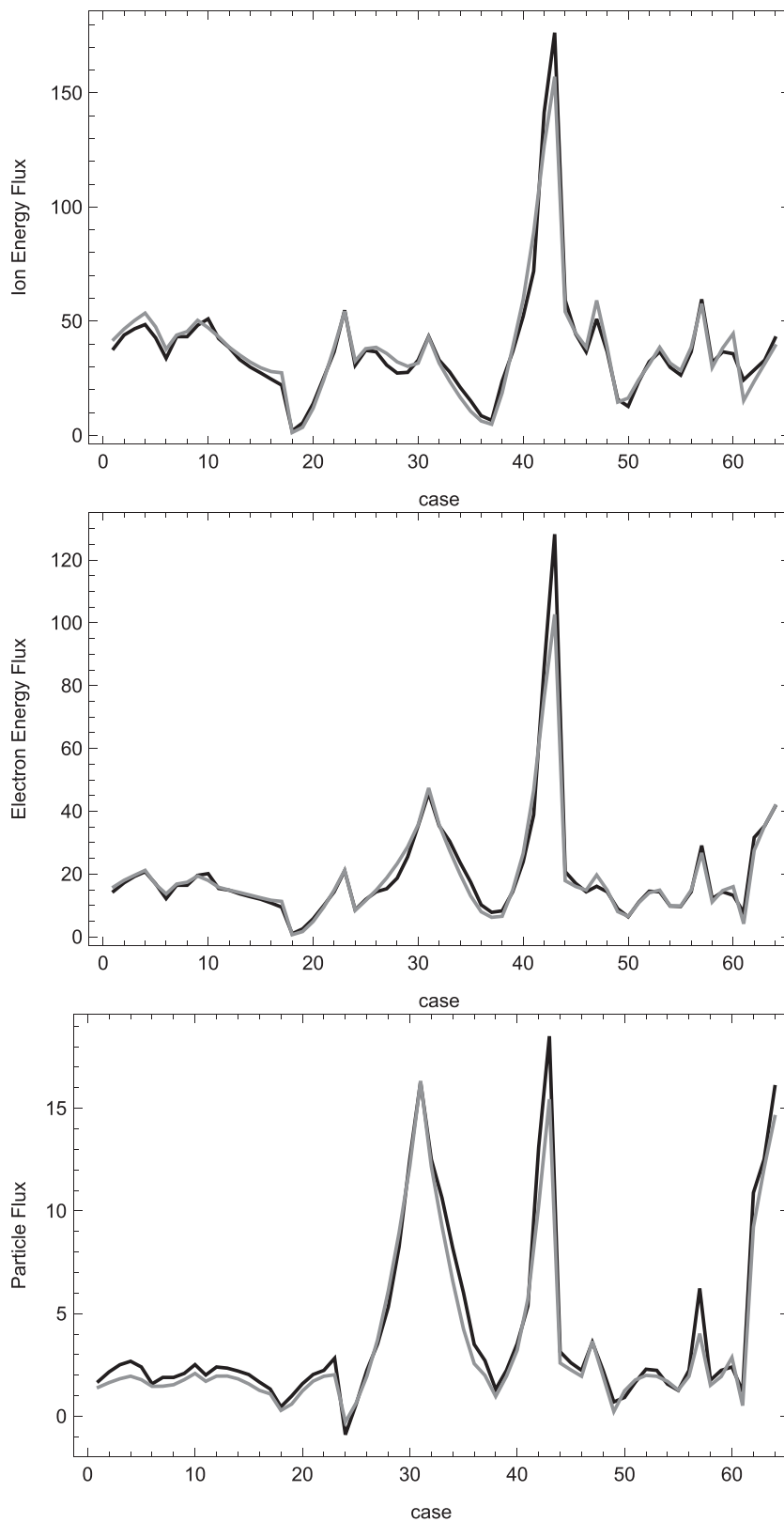


Figure 9. The fluxes for CGYRO (black) and the QLSAT2 model (gray) for all of the cases. Ion energy flux (top), electron energy flux (middle) and particle flux (bottom).

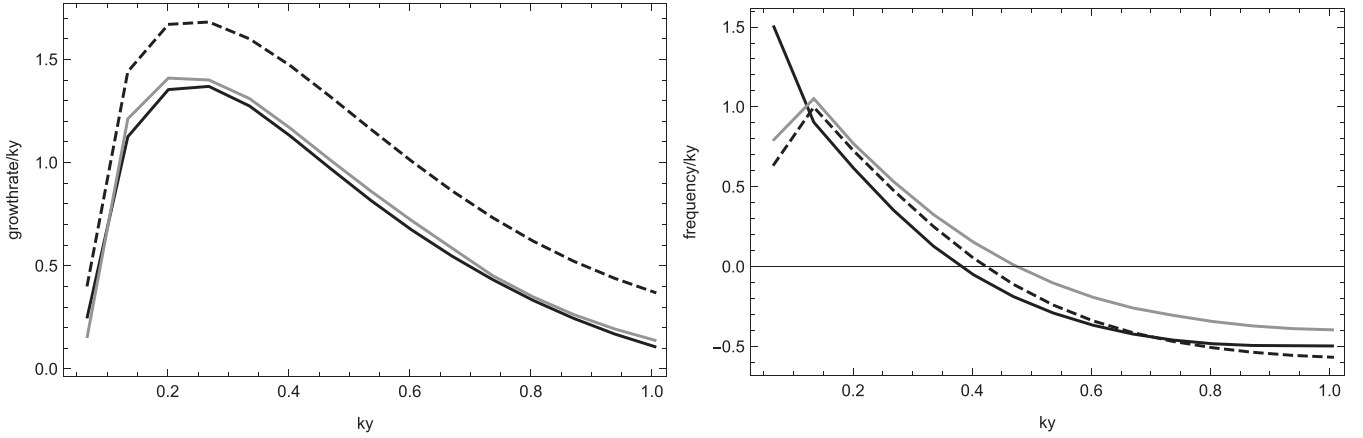


Figure 10. The CGYRO (black) and TGLF for the X2 (dashed) and X3 (gray) collision models linear growth rate/ k_y (left) and frequency/ k_y (right) for the GASTD case with $a/L_{n_e} = a/L_{n_i} = 3.0$.

these 54 cases but a larger database could invalidate it. A finer fit to the shape of the intensity spectrum could also make this overall pressure factor unnecessary.

7. Improvements to the TGLF linear eigensolver

The use of the linear eigenmodes from CGYRO allowed the fitting of a saturation model to the non-linear CGYRO simulations without concern for the accuracy of the linear eigenmodes. The problem with this approach is that the calculation of the linear CGYRO eigenmodes is 18 000 times slower compared to the reduced gyro-fluid model TGLF [4]. The CGYRO linear calculation is also an initial value run so it only finds the most unstable mode, whereas TGLF is a matrix eigensolver that finds all of the unstable branches of its equations. Including subdominant modes is essential for helping the flux smoothly cross branch jumps. Initial value runs have convergence difficulty near the linear stability threshold or when there are two modes with similar growth rates but different frequencies. These issues make it impractical to use CGYRO (or any initial value gyrokinetic code) as the linear eigenmode solver in a transport code.

The linear eigenmodes of TGLF were found to lack accuracy for the high density gradient cases in the database. For example, the spectrum of the growth rate (left) and frequency (right), divided by the poloidal wavenumber k_y for the GASTD case parameters but with higher density gradients ($a/L_{n_e} = a/L_{n_i} = 3.0$) is shown in figure 10. The black curves are the calculation using CGYRO with the Sugama multi-species collision operator. The dashed curves are for TGLF with the collision model of reference [20] (denoted X2 here for option XNU_MODEL = 2). The TGLF equations have bounce averaged trapped particles for all species. The TGLF collision model has only pitch angle scattering of electrons. The dominant term in the TGLF collision model is from the gradient of the distribution function at the trapped-passing boundary which is modeled by ($\xi = v_{\parallel}/v$)

$$\nu_{ee} \frac{d\tilde{f}_e}{d\xi} \Big|_{\xi=\xi_t} = c_b \nu_{ee}^{(1-\sigma_b)} (v_{the} k_{\parallel})^{\sigma_b} \tilde{f}_e. \quad (28)$$

Where $\xi_t = \sqrt{1 - B_{\min}/B_{\max}}$ is the trapped-passing boundary value. For the X2 model $c_b = 0.114$ and $\sigma_b = 0.5$. The linear growth rate in figure 10 for the X2 model (dashed) is too large across most of the spectrum. This 21% larger peak in γ_{k_y}/k_y translates to about 47% larger fluxes for TGLF with the X2 model compared to CGYRO using the saturation model of this paper. Increasing the coefficient c_b of the trapped-passing boundary collision term lowers the linear growth rate at low k_y but this shifts the peak to higher k_y and does not help lower the higher k_y growth rates.

The TGLF equations have a model for the loss of bounce averaging of the Landau resonance by trapped particles [4]. The model attempts to estimate how far into the trapped region of velocity space the particles can experience Landau damping and hence should be part of the circulating particle fluid. Assuming that the Landau resonance condition determines the frequency gives the relation

$$\omega = k_{\parallel} v_{\parallel} = k_{\parallel} R q d\theta/dt. \quad (29)$$

Integrating this equation in time gives $\omega \Delta t = k_{\parallel} R q \Delta \theta$. A trapped particle keeps the same sign of its velocity while traveling between bounce angles θ_B . A minimum requirement for a trapped particle to be able to average the Landau resonance is that it can change the sign of its velocity before the parallel electric field of the wave changes sign. Hence it must travel more than half an orbit ($2\theta_B$) in half a wave period ($\omega \Delta t = \pi$). This gives the condition for a trapped particle to be able to Landau average

$$\Delta \theta = \frac{\pi}{R q k_{\parallel}} > 2\theta_B. \quad (30)$$

This gives a condition for the maximum bounce angle for trapped particles that can average the Landau resonance θ_{LA} [4]

$$\theta_{LA} = \min \left(\frac{\pi}{2R q k_{\parallel}}, \pi \right). \quad (31)$$

The effective boundary for trapped particles that can bounce average the Landau resonance is thus $\xi_{LA} = \sqrt{1 - B_{\min}/B(\theta_{LA})}$. In practice this condition is used in TGLF to reduce the trapped fraction using an estimate

of the parallel wavenumber k_{\parallel} . The eigenvalue solution procedure for TGLF adjust the parallel wavenumber with just a Gaussian wavefunction with the first 2 Hermite polynomials to find the maximum linear growth rate. The wavefunction is then refined with more Hermite polynomials (typically 4). For high magnetic shear, the parallel wavenumber found is larger and the effective trapped particle boundary is reduced. This tracks the linear growth rate for trapped electron modes well [4]. The TGLF problem of too high a linear growth rate at high density gradient is conjectured to be due to the higher density gradient drift frequency ($k_y a / L_{ne}$) causing a loss of bounce averaging. In order to include this effect, the above model is modified in the following way

$$\theta_{aLA} = \min \left(\frac{\pi}{2Rqk_{a\parallel}^{\text{eff}}}, \pi \right) \quad (32)$$

$$k_{a\parallel}^{\text{eff}} = |k_{\parallel}| + 3.0 \frac{B_{\min}}{B_{\max}} \left| \frac{ak_y}{v_{\text{tha}} L_{na}} \right|. \quad (33)$$

The coefficient 3.0 in equation (33) was determined by fitting to the CGYRO linear growth rate spectrum at higher density gradient. The new model for the loss of Landau averaging (equation (33)) is species dependent, since the diamagnetic drift frequency $k_y a / l_{na}$, and the thermal velocity $v_{\text{tha}} = \sqrt{T_a / m_a}$, are species dependent. The trapped ions lose bounce averaging at a lower k_y than the electrons in this model, which makes a difference at the lowest k_y range. The trapped-passing boundary collision model (equation (28)) was adjusted to $c_b = 0.315$, $\sigma_b = 0.34$ in order to match the decay of the CGYRO growth rate spectrum with collisions. This change in the electron collisions and the model for the loss of bounce averaging is the X3 model (option XNU_MODEL = 3). The gray curves in figure 10 show the improvement in the TGLF fit for the X3 model. It was found that this model was good up to about $\nu_{ee} a / c_s = 1.0$. Above this value for the electron collision frequency, the low k_y modes are over-stabilized. A new eigensolver for TGLF that does not employ the bounce averaging approximation is under development. This will eliminate the need for these ad hoc adjustments to bounce averaging.

8. TGLF implementation of the QL model

With the X3 collision model, and the new SAT2 saturation model presented in this paper, TGLF provides a good quasi-linear model of the CGYRO non-linear fluxes in the database. The error between the TGLF fluxes and CGYRO for the scans are shown in figure 11. The RMS average error over all of the scans is: Qi 16.2%, Qe 16.6%, and Γ_e 33.5%. This is not as good as found using the CGYRO eigenvalues but is significantly better than previous saturation models. For example, the SAT1 model [3] (with X2) run on this CGYRO database gives errors: Qi 53.4%, Qe 56.7%, and Γ_e 74.5%. The number of Hermite polynomials for the ballooning mode wavefunction in TGLF was increased from 4 to 6 for the four cases with $q \geq 3$ (cases 57, 60, 61, 64). This reduced the overshoot of the growth rates for these cases. In figure 12 is shown the ion energy (top), electron energy (middle) and particle (bottom) fluxes for all of the cases. Compared to the QL fluxes computed

with CGYRO eigenmodes in figure 9 the TGLF particle flux is reduced, especially for the scan 7 (cases 38–43) that scans the local radius r/a and hence scans the trapped fraction. This suggests a deficit in the trapped electron contribution to the particle flux for TGLF. These fluxes were computed including only the most unstable mode. In transport codes, TGLF includes subdominant eigenmodes so that branch jumps will be smoother. Including up to 4 subdominant modes, with mode intensities reduced by the square of the ratio of the linear growthrate to the most unstable mode at the same k_y , increases the TGLF-SAT2 errors somewhat to: Qi 16.9%, Qe 17.6%, and Γ_e 34.1%. The overall coefficient needs to be reduced by a factor of 0.95 to zero the offset over the whole database.

9. Calibration of the spectral shift model for $E \times B$ velocity shear

The spectral shift model for the effect of equilibrium $E \times B$ velocity shear ($\gamma_{E \times B}$) [19] on gyrokinetic turbulence [2] captures the shift in the peak of the 2D flux surface averaged potential spectrum away from $k_x = 0$ to a finite value k_{x0} . The direction and size of this shift is determined by the $E \times B$ velocity shear. This spectral shift produces an ion stress contribution to momentum transport by breaking the parity of the eigenmode [34]. However, this shift in the eigenmode does not reduce the linear growth rate enough to account for the reduction in the fluxes. The peak of the potential spectrum is reduced by two effects. One is the change in the radial correlation length that was previously identified as a suppression mechanism [35, 36]. This is manifest in the spectral shift model as a change in the width of the radial wavenumber spectrum and a tilt in the radial orientation of the turbulent eddies [34]. This effect alone is too weak to account for the reduction in fluxes with $E \times B$ velocity shear in the turbulence simulations [31]. The second effect is a temporal reduction in the effective mixing rate $\gamma_{k_y}^{\text{eff}}$. Both of these reductions in the peak of the potential were shown [2] to be directly related to the shift k_{x0} . The generalization of the spectral shift model to the 3D spectrum (equation (12)) is given by the formula:

$$\Phi(\theta)_{k_x, k_y} = G(\theta) \frac{\Phi(0)_{0, k_y}}{\left(1 + \left(\frac{k_{x0}}{k_x^{\text{model}}} \right)^2 + \left(\frac{k_x - k_{x0}}{k_x^{\text{model}}} \right)^2 \right) \left(1 + \left(\alpha_x \frac{k_{x0}}{k_x^{\text{model}}} \right)^{\sigma_x} \right)}. \quad (34)$$

Here $\Phi(0)_{0, k_y}$ is the peak of the potential in the absence of equilibrium $E \times B$ velocity shear (same as equation (12)). The left hand factor in the denominator in equation (34) accounts for the broadening of the radial wavenumber spectral width by the spectral shift k_{x0}

$$k_x^{\text{net}} = \sqrt{\frac{\sum_{k_x} (k_x - k_{x0})^2 \Phi^2}{\sum_{k_x} \Phi^2}} = k_x^{\text{model}} \sqrt{1 + \left(\frac{k_{x0}}{k_x^{\text{model}}} \right)^2}. \quad (35)$$

The radial wavenumber spectral width in the absence of equilibrium $E \times B$ velocity shear is given by the model k_x^{model} in equation (21). The additional temporal reduction in the peak amplitude is given by the right hand factor in the denominator

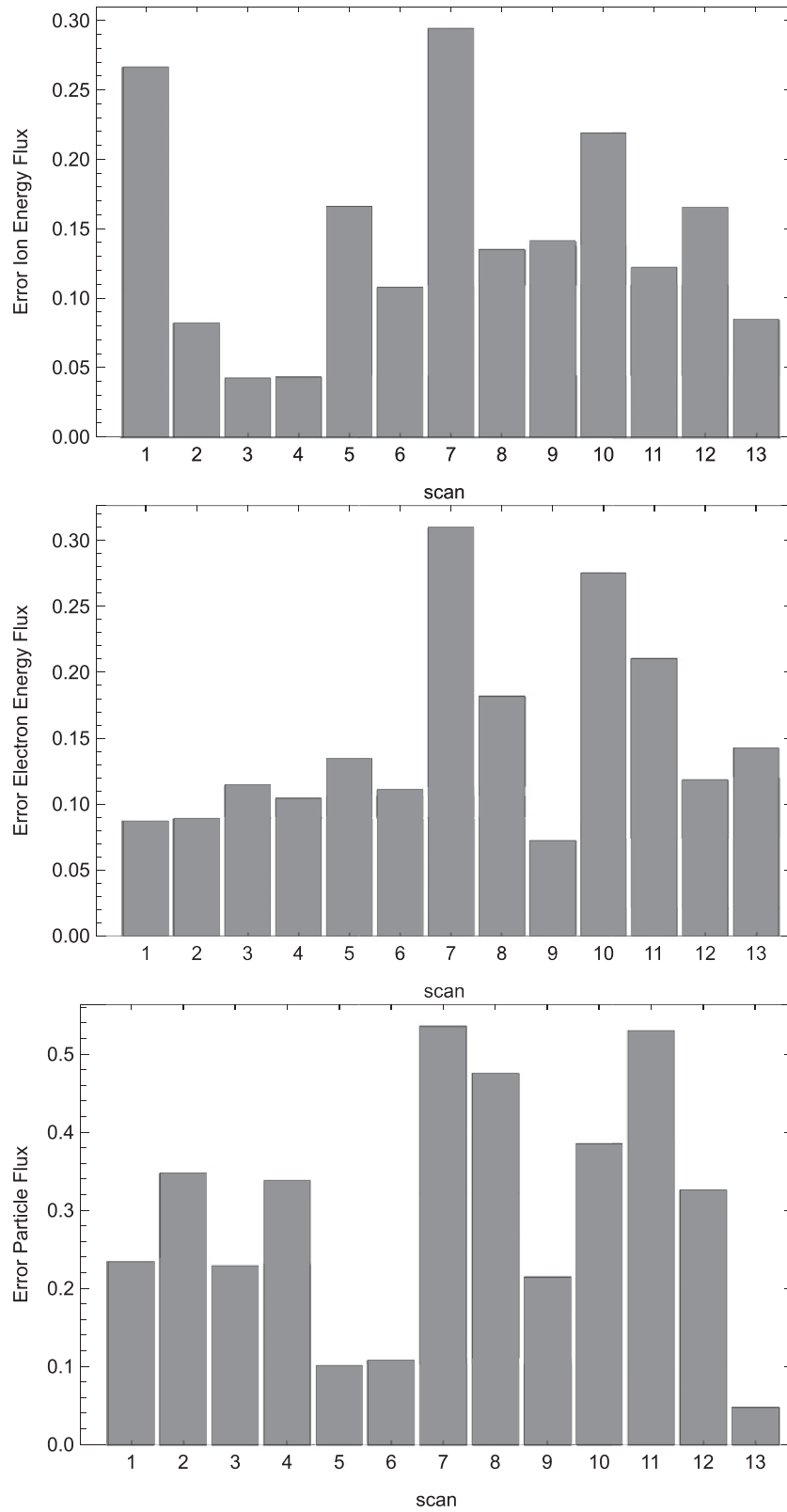


Figure 11. The error between the TGLF fluxes and CGYRO for each scan. Ion energy flux (top), electron energy flux (middle) and particle flux (bottom).

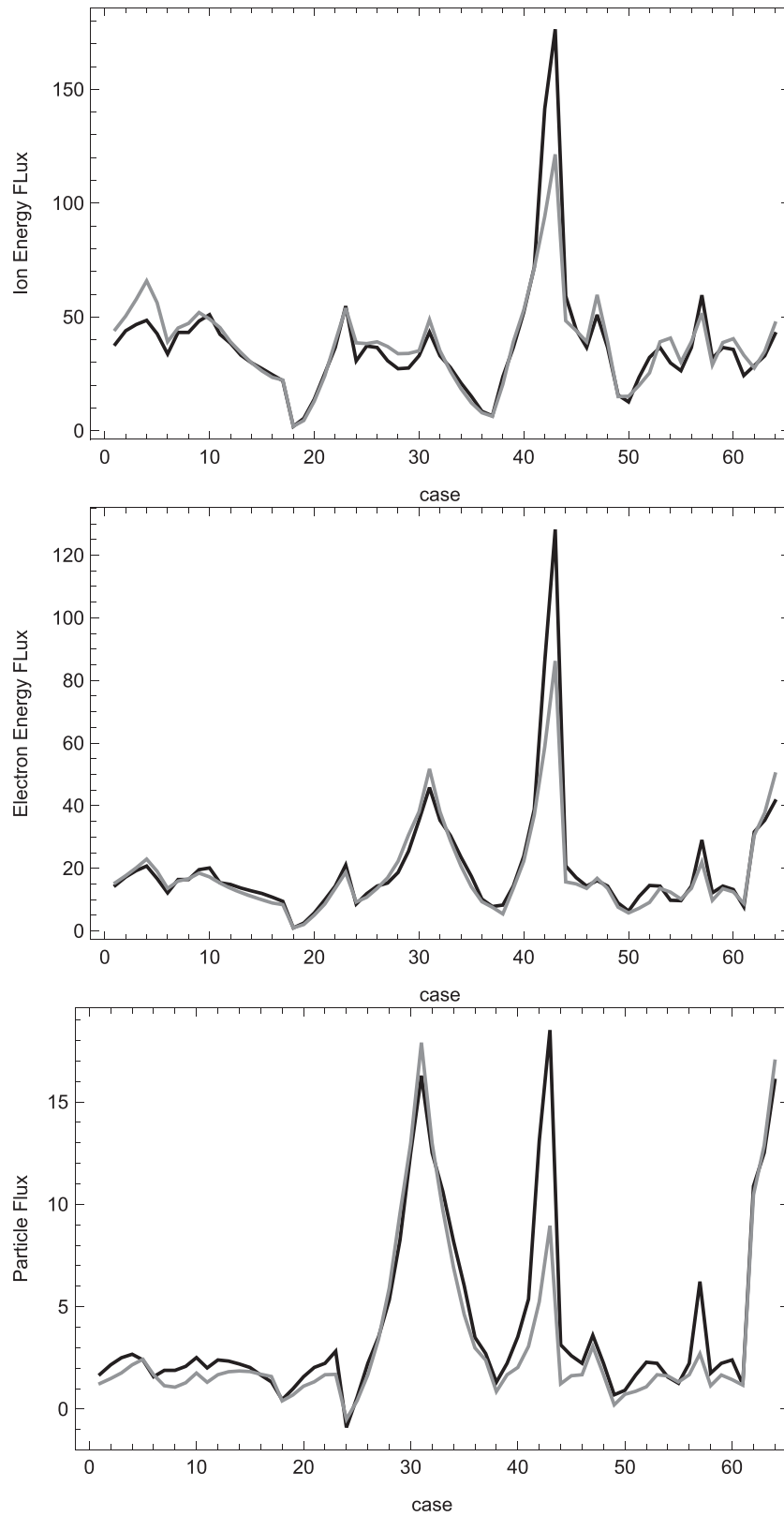


Figure 12. The fluxes for CGYRO (black) and the TGLF model (gray) for all of the cases. Ion energy flux (top), electron energy flux (middle) and particle flux (bottom).

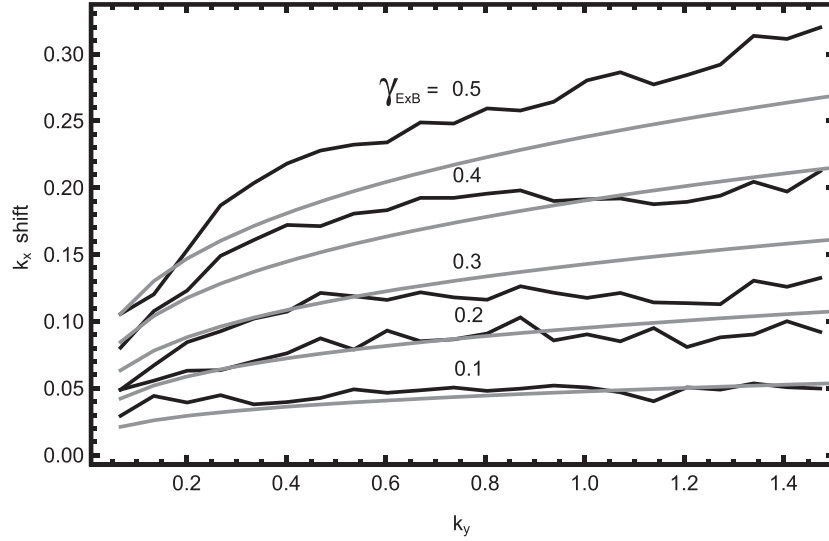


Figure 13. Spectrum of the radial wavenumber shift k_{x0} , computed from CGYRO simulations equation (38) (black), and the model equation (37) (gray), for a range of values of the equilibrium $E \times B$ velocity shear $\gamma_{E \times B}$, for the GASTD case.

of equation (34)

$$\gamma_{k_y}^{\text{net}} = \frac{\gamma_{k_y}}{\left(1 + \left(\alpha_x \frac{k_{x0}}{k_x^{\text{model}}}\right)^{\sigma_x}\right)}. \quad (36)$$

In the original spectral shift model, the formula for the spectral shift k_{x0} that was determined to fit GYRO simulations has a non-linear dependence on the $E \times B$ velocity shear that also depends on the flux surface shape [34]. Fitting to CGYRO simulations with different flux surface shape was carried out and a linear relation was found to be sufficient. This difference is thought to be due to the fact that CGYRO is spectral in k_x so it has higher accuracy for the gyro-averaging operator (Bessel functions) than GYRO which uses a radial grid. It is possible to use a full Fourier transform to obtain spectral accuracy in GYRO but this was not done in the original simulations used to calibrate the spectral shift model due to the computational expense.

Implementing the spectral shift model in TGLF requires two passes. The first pass computes the linear eigenvalue spectra without $E \times B$ velocity shear. The second pass uses these bare linear growth rates to compute the spectral shift k_{x0}^{model} (equation (37)). This spectral shift is then used to recompute the linear shifted ballooning eigenmodes to obtain the quasi-linear weights. The shifted ballooning modes produce a small change in the energy and particle weights but produce all of the phase shift required for the ion stress. In the original spectral shift model, the bare linear growth rate at each k_y was used in the formula for the spectral shift at each k_y . This implementation is still used for the older saturation models (SAT_RULE = 0 or 1).

For the new saturation model of this paper (SAT_RULE = 2) the bare growth rates are used to compute the bare values of $k_{y\text{max}}$ and γ_{max} . The spectral shift spectrum is then computed from the formula:

$$k_{x0}^{\text{model}} = 0.32k_y \left(\frac{k_{y\text{max}}}{k_y}\right)^{0.7} \left(\frac{\gamma_{E \times B}}{\gamma_{\text{max}}}\right). \quad (37)$$

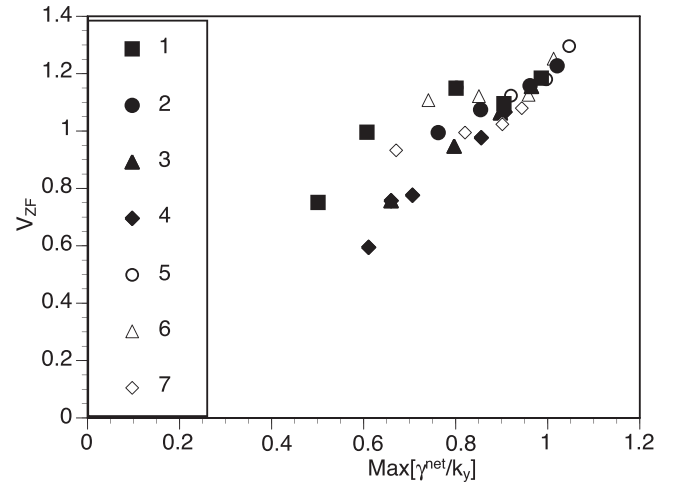


Figure 14. The RMS zonal velocity vs $\max[\gamma_{k_y}^{\text{net}}/k_y]$ (equation (36)) for cases: (1) GASTD $\gamma_{E \times B} = 0, 0.1, 0.2, 0.3, 0.4, 0.5$, (2) $\kappa = 1.25$, $\gamma_{E \times B} = 0, 0.1, 0.2, 0.3$, (3) $\kappa = 1.5$, $\gamma_{E \times B} = 0, 0.1, 0.2, 0.3$, (4) $\kappa = 1.75$, $\gamma_{E \times B} = 0, 0.1, 0.2, 0.3$, (5) $\Delta = -0.1$, $\gamma_{E \times B} = 0, 0.1, 0.2, 0.3$, (6) $\Delta = -0.2$, $\gamma_{E \times B} = 0, 0.1, 0.2, 0.3$, (7) $\Delta = -0.4$, $\gamma_{E \times B} = 0, 0.1, 0.2, 0.3$.

This is a reasonable fit to the spectral shift k_{x0} computed directly from the CGYRO spectra

$$k_{x0} = \frac{\sum_{k_x} |\tilde{\phi}_{k_y, k_x}|^2 k_x}{\sum_{k_x} |\tilde{\phi}_{k_y, k_x}|^2} \quad (38)$$

as shown in figure 13 for the GASTD case.

The model equation (37) is able to fit the spectral shift for a scan in elongation and Shafranov shift without explicit geometry factors. This is a simplification compared to the original model that used the linear bare growth rate to normalize the $E \times B$ velocity shear and required a geometric correction. Next, the bare linear growth rate without $E \times B$ shear is modified by the temporal reduction factor (equation (36)) including

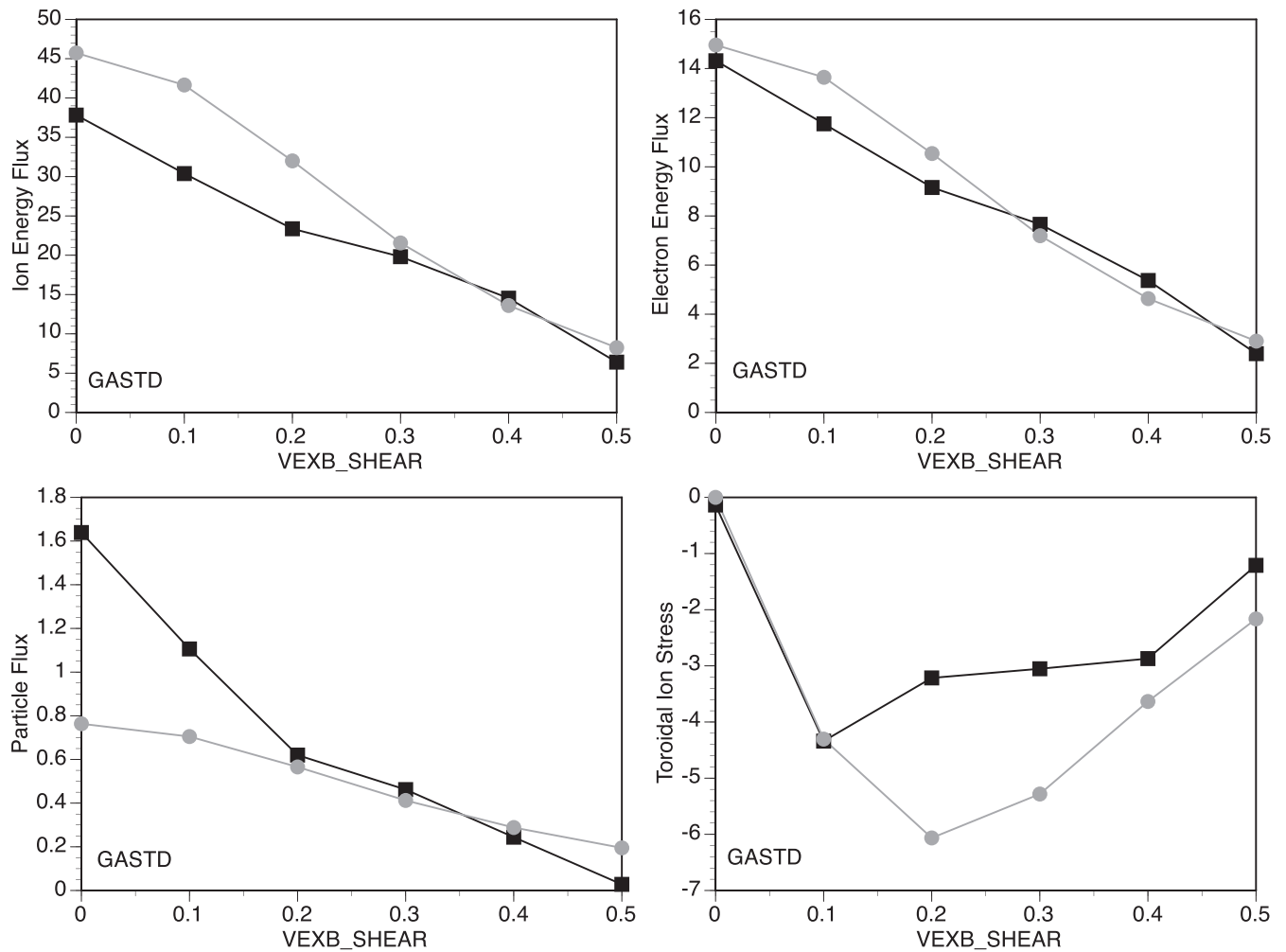


Figure 15. Scan in the equilibrium $E \times B$ velocity shear for the GASTD case. The fluxes for CGYRO (black) and the TGLF model (gray). Ion energy flux (top left), electron energy flux (top right), particle flux (bottom left) and ion toroidal stress (bottom right).

γ_{\max} . This is then used in the saturation model (equation (34)). The net spectral width (equation (35)) is also used in place of the bare spectral width in the saturation formula.

The zonal potential spectrum does not shift but remains symmetric about $k_x = 0$ as it must due to the reality condition on the Fourier amplitudes. The RMS average zonal velocity (equation (9)) is observed to be reduced by the equilibrium $E \times B$ velocity shear. The zonal flow saturation rule remains (equation (8)) approximately true if the temporal reduction factor is applied as shown in figure 14 for the set of 30 cases. The temporal reduction factor was computed using the value of the spectral shift spectrum k_{x0} (equation (38)) computed from the non-linear spectrum and the model equation (21) for the width of the spectrum. This gives about the right level of reduction in zonal flow velocity even though the coefficients $\alpha_x = 1.21$ and $\sigma_x = 2$ were fit to the fluxes not the zonal velocity. This demonstrates that the saturated zonal mixing rate remains in balance with the net effective linear drive as the turbulence is suppressed by the equilibrium $E \times B$ velocity shear.

A novel method for including equilibrium $E \times B$ velocity shear in a periodic flux tube was used for these simulations [30]. The equilibrium $E \times B$ velocity is introduced as a sawtooth waveform over the radial periodic box. The magnitude of the flow shear is the same everywhere but the sign flips at the peaks of the sawtooth pattern. This sign flip has no effect on the energy and particle fluxes but reverses the sign of the toroidal stress. The toroidal stress is computed in the central zone of the flux tube where the $E \times B$ velocity shear has one sign. The shift in the radial wavenumber spectrum is also computed in this same zone. A good agreement between the k_x spectral code CGYRO using this method and GYRO using a radial grid was shown in reference [30] for the GASTD case with adiabatic electrons. The CGYRO results in figure 15 are in good agreement with the GYRO results of reference [2] for the GASTD case with kinetic electrons but the reduction in the energy fluxes is greater at higher shear for GYRO than CGYRO.

Using the model for the spectral shift (equation (37)) a good fit to the energy and particle fluxes is obtained for parameters $\alpha_x = 1.21$, $\sigma_x = 2$. Note that this is significantly different than the fit to GYRO simulations [2] with $\alpha_x = 1.15$, $\sigma_x = 4$.

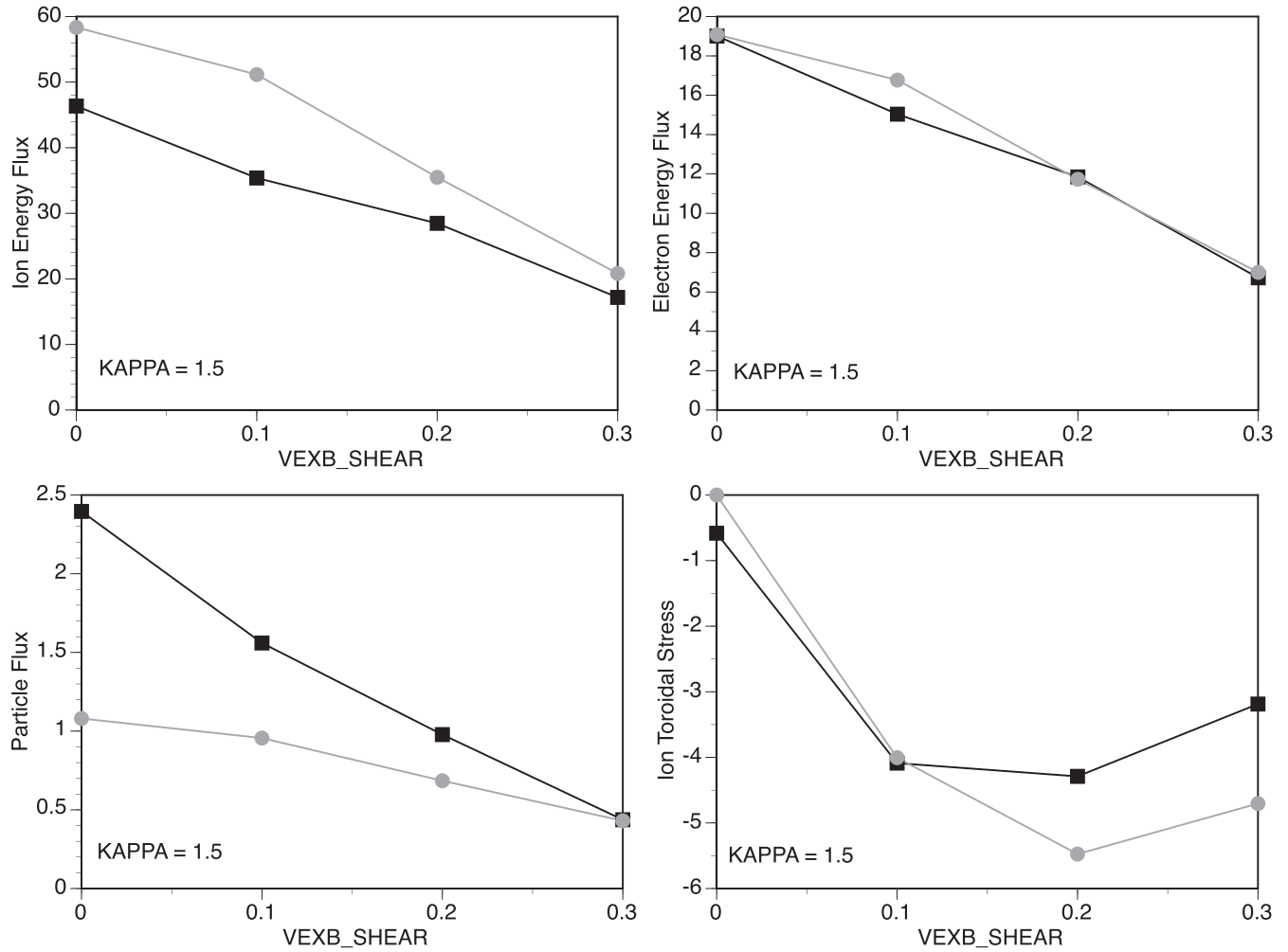


Figure 16. Scan in the equilibrium $E \times B$ velocity shear for Elongation (KAPPA) 1.5. The fluxes for CGYRO (black) and the TGLF model (gray) for the GASTD case. Ion energy flux (top left), electron energy flux (top right), particle flux (bottom left) and ion toroidal stress (bottom right).

This new CGYRO fit is only used for the new saturation model (SAT_RULE = 2) in TGLF.

The shift in the ballooning mode radial wavenumber, that produces the stress, was found to require a multiplier $G_x = -\text{sign}(B_T)0.7/|\nabla r|_0^2$ times k_{x0}^{model} in order to better track the Shafranov shift dependence of the toroidal stress. Note that TGLF and CGYRO have opposite conventions for the direction of the toroidal angle. The CGYRO (black) and TGLF (gray) ion energy flux (top left), electron energy flux (top right), particle flux (bottom left) and ion toroidal stress (bottom right) scans in the equilibrium $E \times B$ velocity shear are shown for the GASTD case in figure 15, and cases with elongation $\kappa = 1.5$ in figure 16 or with Shafranov shift $\Delta = -0.2$ in figure 17.

The impact of the shear in the $E \times B$ Doppler shift has been treated separate from the parallel velocity shear that enters the gyrokinetic equation as another instability drive. The parallel velocity and parallel velocity shear also cause symmetry breaking phase shifts that interacts with the $E \times B$ Doppler shift shear. There is no tuning of the TGLF linear equations required for these parallel flow terms.

10. Calibration of the multi-scale model for electron scale energy transport

The final step in the calibration of TGLF with the new saturation model is to extend the model to electron scales. The multi-scale simulations of an Alcator C-MOD L-mode plasma by Howard [26] with the GYRO code were used to formulate the first multi-scale saturation model [3] (SAT_RULE = 1). The ion-scale sector of this model is replaced by the new model of this paper. The electron scale modes were found to be suppressed by the zonal flow mixing limiting the effective non-linear mixing rate to the ion scale γ_{max} for $k_y \geq k_{y\text{max}}$ as in equation (22). However, if the electron scale peak of γ_{k_y}/k_y is larger than the ion scale peak, the electron scale contribution to the potential can increase yielding a larger contribution to the electron energy flux for $k_y \geq 1$. This effect is visible in figure 18 where the GYRO (black) and TGLF-SAT2 (gray) electron energy flux (squares), ion energy flux (circles) and the contribution to the electron energy flux from electron scales ($k_y \geq 1$) (triangles) are shown for scans in the ITG (left) and electron temperature gradient

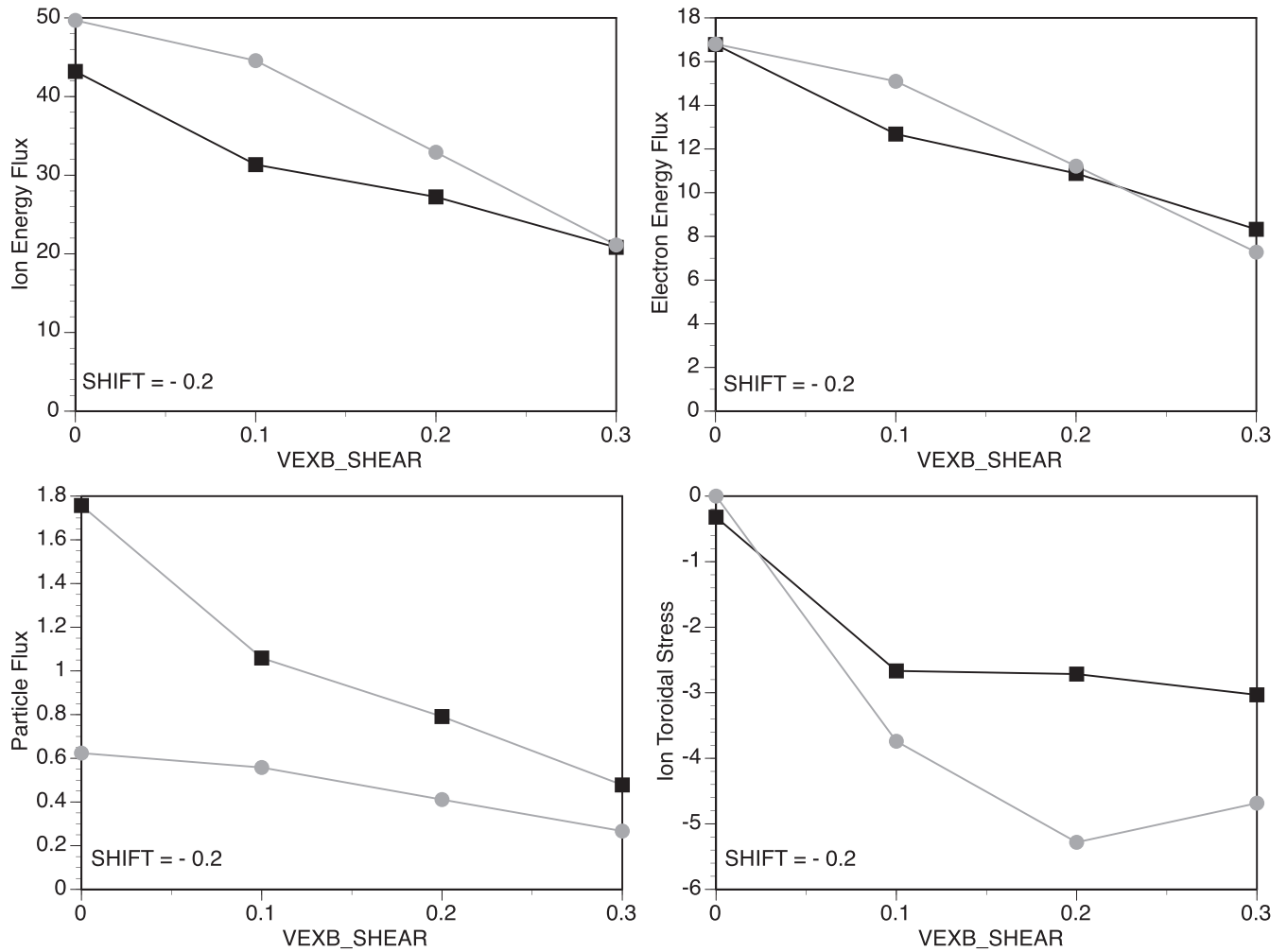


Figure 17. Scan in the equilibrium $E \times B$ velocity shear for Shafranov shift (SHIFT) -0.2 . The fluxes for CGYRO (black) and the TGLF model (gray) for the GASTD case. Ion energy flux (top left), electron energy flux (top right), particle flux (bottom left) and ion toroidal stress (bottom right).

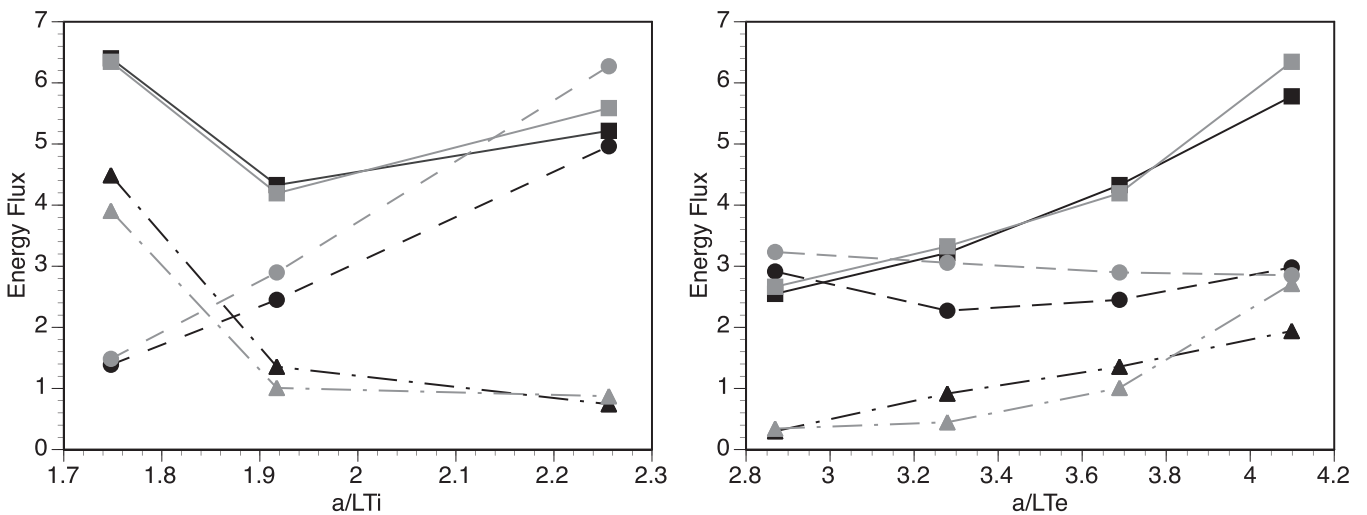


Figure 18. Scan in the equilibrium ion (left) and electron (right) temperature gradients for multi-scale GYRO simulations of a C-MOD L-mode [26]. The energy fluxes for GYRO (black) and the TGLF model (gray). Ion energy flux (circle), electron energy flux (square) and electron-scale electron energy flux (triangles).

(right) about an L-mode discharge on the C-MOD tokamak [26]. The increase in the electron scale energy flux as the ion temperature gradient is lowered (left panel) is due to the zonal flow mixing rate ($V_{ZF}k_y$) lowering below the linear growth rate at electron scales. This effect is built into the saturation model for $k_y \geq k_{y\max}$ by changing the formula equation (22) to:

$$\gamma_{k_y}^{\text{model}} = b_2(\gamma_{\max} + \max[\gamma_{k_y} - \alpha_{ZF}k_y V_{ZF}, 0.0]). \quad (39)$$

The TGLF fluxes with the new saturation model use this formula with $\alpha_{ZF} = 1.05$. The electron-scale saturation model includes a Lorentz distribution weighted average over k_y of $\gamma_{k_y}^{\text{model}}$ [3]. This represents the effect of the non-linear mixing between modes with different k_y . In the original SAT1 model, a change in the scaling of the width of the radial wavenumber spectrum for $k_y \geq 1.0$ was included. The new model accounts for this anisotropy of the spectral width through the geometric factors in equations (16) and (21). The original multi-scale GYRO runs output flux surface averaged potential fluctuation spectra so the poloidal angle dependence is unknown. New multi-scale simulations are needed to verify that the poloidal angle dependence of the new model is correct at electron scales. The agreement of the TGLF fluxes with GYRO in figure 18 is very good. These C-MOD simulations include an impurity ion, shaped flux surfaces, and a low amount of equilibrium $E \times B$ velocity shear [26, 27].

11. Summary

A new, more accurate, quasi-linear saturation model (SAT2) has been verified and calibrated to a database of CGYRO turbulence simulations in this paper. The model began with exploring the 3D structure of the saturated potential fluctuation spectrum in a previous paper [1]. The SAT2 model was constructed using the linear growth rate and quasi-linear weights from the spectrum of the most unstable modes computed with the same code as the non-linear turbulence simulations. The saturation model is fit to the poloidal wavenumber spectrum of the intensity required to make the quasi-linear approximation to the electron energy flux exact (QL intensity). It was demonstrated that the quasi-linear weights accurately predict the ratio of the ion energy and particle fluxes to the electron energy flux. This quantitative test showed that quasi-linear weights contribute 5.4% of the error in the quasi-linear ion energy fluxes averaged over the whole database of 13 CGYRO scans. The quasi-linear weights contribute 19.8% error to the particle flux due to lower quasi-linear fluxes at low density gradient than from the turbulence. The SAT2 model for the quasi-linear intensity introduces additional error to the quasi-linear fluxes. The fractional error in the quasi-linear fluxes for the 13 scans is 10.5% for ion energy, 10.9% for electron energy, and 18.9% for particle flux. These errors are lower than previous saturation models fit to gyrokinetic simulations [3, 14].

A central part of the SAT2 model (equation (14)) spectral shape and peak intensity is the zonal flow mixing rule (equation (8)) for the saturation of the zonal potential fluctuations. It was shown to be quite accurate for the whole database in figure 3. It was also shown that the static zero frequency

component of the zonal potential is a small contributor to the RMS zonal velocity for most cases. The zonal flow mixing rule was shown to work for cases with an equilibrium $E \times B$ velocity shear if γ_{\max} is modified by the spectral shift model (equation (36)). The other central element of the SAT2 model is the width of the radial wavenumber spectrum. It is conjectured that the spectral width is determined by the zonal potential mediated coupling of different radial wavenumbers for the same poloidal wavenumber. It was found in this larger database that the width of the zonal potential spectrum (equation (11)) is more variable than previously observed in reference [1]. This deserves further study to understand the physical mechanisms at work. The observed broadening of the radial wavenumber spectral width at low k_y causes a reduction in the intensity of the turbulence. Including this effect in the SAT2 model allowed for a simplification of the model compared to its predecessor SAT1 [3] while giving a better fit to the quasi-linear intensity at low poloidal wavenumber.

The saturation model is an independent component of a quasi-linear approximation to transport fluxes that can be used with any model for gyrokinetic linear stability to compute quasi-linear fluxes. In this paper, the SAT2 model was implemented in the TGLF quasi-linear model after improvements to the linear eigenmode accuracy were made. The average fractional error for the 13 scans is 16.2% for ion energy, 16.6% for electron energy, and 33.5% for particle fluxes for TGLF with the SAT2 model and the improved linear eigenmodes.

The spectral shift model for the impact of equilibrium $E \times B$ velocity shear on transport [2] was recalibrated for the SAT2 model. Additional CGYRO scans of the $E \times B$ velocity shear for seven starting cases with different geometry were used for this calibration (30 cases, 23 not in table 1). It was found that the original model could be simplified to a linear relation between the shift in the radial wavenumber spectrum (eddy tilt) and the $E \times B$ velocity shear. This linear model equation (37) fits the CGYRO spectrum of the radial wavenumber shift more accurately than the original non-linear SAT1 model.

The model for the suppression of electron scale turbulence by zonal flow mixing [3] was also recalibrated to the original multi-scale GYRO simulations [26]. The anisotropy between the radial and poloidal wavenumbers (ETG streamers) due to geometric effects in the SAT2 model was found to be sufficient to enhance the electron scale fluxes without the need for modification. The coefficient $\alpha_{ZF} = 1.05$ of the zonal flow mixing term (equation (39)) was hardly changed from unity.

With the recalibration of TGLF, the SAT2 model is now a public option in the TGLF quasi-linear code (SAT_RULE = 2). This option automatically includes the geometry modifications and the changes to the electron collision and bounce averaging model.

Disclaimer

This report was prepared as an account of work sponsored by an agency of the United States Government. Neither the United States Government nor any agency thereof, nor any of their employees, makes any warranty, express or

implied, or assumes any legal liability or responsibility for the accuracy, completeness, or usefulness of any information, apparatus, product, or process disclosed, or represents that its use would not infringe privately owned rights. Reference herein to any specific commercial product, process, or service by trade name, trademark, manufacturer, or otherwise, does not necessarily constitute or imply its endorsement, recommendation, or favoring by the United States Government or any agency thereof. The views and opinions of authors expressed herein do not necessarily state or reflect those of the United States Government or any agency thereof.

Acknowledgments

Discussions with N. Bonanomi, J. Citrin, P. Mantica and R. Waltz contributed to this work. Special thanks to the T17-07 modeling group at JET and the TRANSP team at PPPL for beta testing the new TGLF-SAT2 model. This work was supported by the U.S. Department of Energy under DE-SC0019736, DE-SC0018990, DE-FG02-95ER54309, DE-FC02-06ER54873, and DE-FC02-04ER54698. The research used resources of the Oak Ridge Leadership Computing Facility under Contract DE-AC05-00OR22725 via an award of computer time provided by the ALCC program.

Appendix A. Transformation properties of the quasi-linear fluxes

The transformation properties of quasi-linear models have a subtlety that has not previously been discussed in the literature. The gyrokinetic codes typically evolve the Fourier transform of the fields and distribution function. This necessitates the introduction of the interval ΔK_{iy} in the quasi-linear model for the intensity (equation (5)). It will be shown in this appendix that this factor needs to be defined in a particular way in order for the quasi-linear fluxes to transform in the same way as the non-linear gyrokinetic fluxes for any arbitrary system of normalizations.

For simplicity, consider only the Fourier transform of the angle α defined such that $\mathbf{B} \cdot \nabla \alpha = 0$ [15] and $(\nabla \alpha \cdot \nabla r)_{\theta=0} = 0$:

$$\tilde{\phi}(\alpha) = \sum_{n=-N_\alpha}^{N_\alpha} \tilde{\phi}_n e^{-in\alpha} \quad (\text{A.1})$$

$$\tilde{\phi}_n = \int_0^{2\pi} \frac{d\alpha}{2\pi} \tilde{\phi} e^{in\alpha}. \quad (\text{A.2})$$

The gyro-kinetic equation does not have an explicit dependence on the mode number 'n'. The perpendicular wavenumber normalized to the full magnetic field strength in the gyro-average operator (Bessel function) is the physical normalized wavenumber of the turbulence. For a pure ion plasma, with adiabatic electrons, the physical units are the ion temperature, mass and charge, and the magnetic field strength: T_i, m_i, Z_i, B . From these are derived the ion thermal velocity $v_{\text{thi}} = \sqrt{2T_i/m_i}$, the ion gyro-frequency, $\Omega_i = Z_i e B / (m_i c)$, and the ion gyro-radius $\rho_i = v_{\text{thi}} / \Omega_i$. The normalized poloidal wavenumber that is the argument of the

Bessel functions at the outboard midplane for $k_x = 0$ is given by

$$K_{iy} = n \rho_i |\nabla \alpha|_{\theta=0} = \left(\frac{n \rho_i B}{R B p} \right)_{\theta=0}. \quad (\text{A.3})$$

The square amplitude of the Fourier coefficients of the potential fluctuations scales with the interval between ion poloidal wavenumbers (ΔK_{iy}). This property follows from Parseval's theorem

$$\int_0^{2\pi} \frac{d\alpha}{2\pi} |\tilde{\phi}|^2 = \sum_{n=-N_\alpha}^{N_\alpha} |\tilde{\phi}_n|^2. \quad (\text{A.4})$$

A change in the number of mode numbers N_α for a fixed range of poloidal wavenumber $K_{iy\text{max}} = K_{iy}|_{n=N_\alpha}$ requires the Fourier square amplitude to scale like $1/N_\alpha$ to maintain the same sum. This scaling is made explicit by defining an intensity function I by the formula:

$$|\tilde{\phi}_n|^2 = \Delta K_{iy} I(K_{iy}). \quad (\text{A.5})$$

In the continuum limit we have

$$\int_0^{2\pi} \frac{d\alpha}{2\pi} |\tilde{\phi}|^2 = \sum_{n=-N_\alpha}^{N_\alpha} \Delta K_{iy} I(K_{iy}) \approx \int_{-K_{iy\text{max}}}^{K_{iy\text{max}}} dK_{iy} I(K_{iy}). \quad (\text{A.6})$$

The intensity function $I(K_{iy})$ is a function of the ion poloidal wavenumber and so are the linear eigenvalues and quasilinear weights. The ion units are the physical system of units set by the gyro-averaging. Transforming to a new poloidal wavenumber k_{0y} for an arbitrary system of units: T_0, m_0, Z_0, B_0 with $\rho_0 = c \sqrt{m_0 T_0} / (Z_0 e B_0)$ and

$$k_{0y} = \frac{n q \rho_0 B_0}{r B_{\text{unit}}} \quad (\text{A.7})$$

gives the transformation

$$K_{iy} = \alpha_i \frac{k_{0y}}{|\nabla r|_0} = \beta_i k_{0y}, \quad (\text{A.8})$$

where

$$\alpha_i = \sqrt{\frac{2m_i T_i Z_0^2}{m_0 T_0 Z_i^2}}. \quad (\text{A.9})$$

In these new units Parseval's theorem becomes

$$\int_0^{2\pi} \frac{d\alpha}{2\pi} |\tilde{\phi}|^2 = \int_{-k_{0y\text{max}}}^{k_{0y\text{max}}} \beta_i dk_{0y} I(\beta_i k_{0y}). \quad (\text{A.10})$$

This shows that the correct interval to use in the definition of the quasi-linear intensity equation (5) is

$$\Delta K_{iy} = \frac{\alpha_i}{|\nabla r|_0} \Delta k_{0y} \quad (\text{A.11})$$

for any system of units. The CGYRO system of units is given by: $T_0 = T_e, m_0 = m_D, Z_0 = 1, B_0 = B_{\text{unit}}$. Thus for the CGYRO units $\alpha_i = \sqrt{2T_i m_i / (T_e m_D Z_i^2)}$. This factor is confirmed to be correct by the agreement of the quasilinear fluxes with CGYRO for the scan in T_i/T_e (scan 9).

It can be shown that the product $I_{ky}^{\text{model}} \mathbf{W} Q_{ky}$ scales in the expected gyro-Bohm way for the energy flux in changing

from one system of units to another. The summation measure equation (A.11) does not alter the overall scaling of the fluxes since it is the same for any system of units. This summation measure (equation (A.11)) was used in the fitting of the geometry factors [1].

In a mixed ion plasma it is not clear what ‘main ion’ should be used. A more general summation measure is

$$\Delta K_{iy} = \frac{\Delta k_y}{k_{y\max}}. \quad (\text{A.12})$$

This measure is independent of the system of units and is equivalent to equation (A.11) for a single ion plasma because the value of $k_{y\max}$ where the maximum of γ_{ky}/k_y occurs has the property that $k_{y\max} \alpha_i / |\nabla r|_0$ is invariant under a change of external units. Using this more general summation measure (equation (A.12)) improves the fit of the model by tracking the magnetic shear and safety factor better due to shifts in $k_{y\max}$. Using this new measure requires some adjustments to the fitting parameters: b_0 changed from 0.72 to 0.76, b_3 changed from 2.4 to 1.0, and the parameter d_1 is now divided by a factor of $|\nabla r|_0$. The fit to the elongation and Shafranov shift scans (1 and 2) is about the same as before with these adjustments.

ORCID iDs

G.M. Staebler  <https://orcid.org/0000-0002-1944-1733>

J. Candy  <https://orcid.org/0000-0003-3884-6485>

B. Patel  <https://orcid.org/0000-0003-0121-1187>

References

- [1] Staebler G.M., Candy J., Belli E.A., Kinsey J.E., Bonanomi N. and Patel B. 2020 *Plasma Phys. Control. Fusion* **63** 015013
- [2] Staebler G., Waltz R., Candy J. and Kinsey J. 2013 *Phys. Rev. Lett.* **110** 055003
- [3] Staebler G.M., Candy J., Howard N.T. and Holland C. 2016 *Phys. Plasmas* **23** 062518
- [4] Staebler G.M., Kinsey J.E. and Waltz R.E. 2005 *Phys. Plasmas* **12** 102508
- [5] Weiland J., Jarmén A.B. and Nordman H. 1989 *Nucl. Fusion* **29** 1810
- [6] Waltz R.E., Casati A. and Staebler G.M. 2009 *Phys. Plasmas* **16** 072303
- [7] Casati A. *et al* 2009 *Nucl. Fusion* **49** 085012
- [8] Told D., Jenko F., Görler T., Casson F.J. and Fable E. 2013 *Phys. Plasmas* **20** 122312
- [9] White A.E. *et al* 2010 *Phys. Plasmas* **17** 056103
- [10] Antonsen T.M. and Lane B. 1980 *Phys. Fluids* **23** 1205
- [11] Kotschenreuther M. 1995 *Bull. Am. Phys. Soc.* **88** 128
- [12] Nordman H., Weiland J. and Jarmén A. 1990 *Nucl. Fusion* **30** 983
- [13] Waltz R.E., Staebler G.M., Dorland W., Hammett G.W., Kotschenreuther M. and Konings J.A. 1997 *Phys. Plasmas* **4** 2482
- [14] Kinsey J.E., Staebler G.M. and Waltz R.E. 2008 *Phys. Plasmas* **15** 055908
- [15] Candy J., Belli E.A. and Bravenec R.V. 2016 *J. Comput. Phys.* **324** 73–93
- [16] Candy J., Borba D., Berk H.L., Huysmans G.T.A. and Kerner W. 1997 *Phys. Plasmas* **4** 2597
- [17] Kinsey J.E., Staebler G.M. and Petty C.C. 2010 *Phys. Plasmas* **17** 122315
- [18] Miller R.L., Chu M.S., Greene J.M., Lin-Liu Y.R. and Waltz R.E. 1998 *Phys. Plasmas* **5** 973
- [19] Waltz R.E. and Miller R.L. 1999 *Phys. Plasmas* **6** 4265
- [20] Staebler G.M. and Kinsey J.E. 2010 *Phys. Plasmas* **17** 122309
- [21] Dimits A.M. *et al* 2000 *Phys. Plasmas* **7** 969
- [22] Belli E.A., Candy J. and Waltz R.E. 2019 *Phys. Plasmas* **26** 082305
- [23] Sugama H., Watanabe T.-H. and Nunami M. 2009 *Phys. Plasmas* **16** 112503
- [24] Freethy S.J. *et al* 2018 *Phys. Plasmas* **25** 055903
- [25] Dannert T. and Jenko F. 2005 *Phys. Plasmas* **12** 072309
- [26] Howard N.T., Holland C., White A.E., Greenwald M. and Candy J. 2016 *Nucl. Fusion* **56** 014004
- [27] Howard N.T., Holland C., White A.E., Greenwald M., Candy J. and Creely A.J. 2016 *Phys. Plasmas* **23** 056109
- [28] Weigl A., Peeters A.G., Rath F., Seiferling F., Buchholz R., Grosshauser S.R. and Strintzi D. 2018 *Phys. Plasmas* **25** 072305
- [29] Austin M.E. *et al* 2006 *Phys. Plasmas* **13** 082502
- [30] Candy J. and Belli E.A. 2018 *J. Comput. Phys.* **356** 448–57
- [31] Waltz R.E., Kerbel G.D., Milovich J. and Hammett G.W. 1995 *Phys. Plasmas* **2** 2408
- [32] Waltz R.E., Austin M.E., Burrell K.H. and Candy J. 2006 *Phys. Plasmas* **13** 052301
- [33] Colyer G.J., Schekochihin A.A., Parra F.I., Roach C.M., Barnes M.A., Ghim Y.-c. and Dorland W. 2017 *Plasma Phys. Control. Fusion* **59** 055002
- [34] Staebler G.M., Candy J., Waltz R.E., Kinsey J.E. and Solomon W.M. 2013 *Nucl. Fusion* **53** 113017
- [35] Shaing K. and Crume E. 1989 *Phys. Rev. Lett.* **63** 2369
- [36] Hahm T.S. 1994 *Phys. Plasmas* **1** 2940